

Strain induced topological phase transitions in split and line graphs of bipartite lattices featuring flat bands ^a

Shivam Sharma ¹ and Amartya S. Banerjee ^{2, †}

¹*Department of Aerospace Engineering and Mechanics,
University of Minnesota, Minneapolis, MN 55455*

²*Department of Materials Science and Engineering,
University of California, Los Angeles, CA 90095, USA*

Abstract

In recent years, materials with topological flat bands have attracted significant attention due to their association with extraordinary transport properties and strongly correlated electrons. This includes phenomena such as high-temperature superconductivity, magnetism, Wigner crystallization, and Mott-insulating behavior. Among these systems, two-dimensional (2D) materials are particularly compelling as they can host electronic states with unique band structures, such as dispersionless states alongside linearly dispersive Dirac cones. In this work, we use tight-binding models to comprehensively investigate a class of 2D lattices that generically support flat bands, and focus on the effects of strain on their electronic and topological properties. The studied lattices are constructed within a unifying graph-theoretic framework, whereupon split-graph and line-graph operations on bipartite square and hexagonal lattices are employed to generate new structures. In the absence of strain, the introduction of spin-orbit coupling (SOC) induces a bulk excitation gap, which transforms flat bands into quasi-flat bands with topologically nontrivial characteristics. By tuning system parameters and external strain, we observe the emergence of directional flat bands, and tilted and semi-Dirac cones. Remarkably, all lattices studied show phase transitions among trivial insulating, semimetallic, and topological phases. Our results highlight the potential of strain engineering as a versatile tool for manipulating electronic and topological phases in a wide variety of 2D materials.

^a Dedicated to Prof. Richard D. James on his 70th birthday.

[†] asbanerjee@ucla.edu

I. INTRODUCTION

Advancements in the design, synthesis and characterization of low dimensional nanomaterials and nanostructures with exotic electronic band structure have garnered significant attention in contemporary research. These materials can exhibit remarkable and unconventional physical properties, paving the way for promising applications in quantum technologies, spintronic devices, and next-generation microelectronics [1–6]. A famous example in two-dimensions (2D) is graphene, where the linearly dispersive Dirac bands leads to unorthodox electronic [7], optical [8], transport[9] and topological properties [10]. Recent developments in the field of many-body condensed matter physics — e.g. observation of dispersion-less states in magic angle twisted bilayer graphene (TBLG)[11, 12] — have underlined the crucial role of flat bands in hosting emergent strongly correlated electronic phenomena such as superconductivity, magnetism, Wigner crystallization and zero-magnetic-field fractional quantum Hall effect [13–30]. This has sparked surge of interest not only in theoretical explanation of superconductivity in such materials [31–33] but also in exploring novel flat bands systems in various platforms such as in bulk materials[34–39], twisted bilayer transition metal dichalcogenides [40], photonic systems[41–48], quantum circuits[49] and ultracold atoms [50, 51]. A particularly interesting thread of research to have emanated is the exploration of such states in quasi-one-dimensional (1D) materials, such as collapsed nanotubes [52–54] or ones with specialized unit cells [55, 56]. The study of these latter systems have been made possible through recently developed symmetry adapted electronic structure calculation techniques [57–62].

Based on insights from the Ginzburg-Landau theory [63], it has been understood that in flat bands systems, the electrons have quenched kinetic energy and become localized resembling atomic-like orbitals. This localization results in a vanishing superfluid weight, implying the absence of superconductivity. However, it was recently shown that non-trivial topology of the Bloch wave function of flat band can preserve the superfluid weight by imposing a lower bound on superfluid density with a non-zero Chern number [64], thereby enabling dissipation-less transport. Moreover, more exotic type of geometrical contribution (i.e. fragile topology) to superfluid weight has been shown for TBLG [65–69] and also explored

experimentally[70]. This underscores the critical role of both topology and strong electronic correlation for realizing novel quantum phenomena [71, 72].

Interest in the topological theory to classify emergent quantum phases of matter began nearly four decades ago, driven by studies on the quantum Hall effect [73] and polyacetylene [74, 75]. The research in this area increased significantly, when it was realized that spin-orbit coupling (SOC) can lead to topological insulating electronic phases [76–78] which were subsequently observed in real materials [79]. Topological insulators (TIs) have SOC induced bulk energy gap, which is topologically distinct from the ordinary (trivial) insulators. These two phases are distinguished by the \mathbb{Z}_2 invariant which is associated with the bulk band structure. An ordinary insulator is a \mathbb{Z}_2 -even phase and can be adiabatically (continuously) deformed into an atomic insulator. It is characterized by strictly localized orbitals or exponentially localized Wannier function. In contrast, the “topological” state is \mathbb{Z}_2 -odd and shows obstruction from any Wannier representation [80]. The TI phase in 2D materials is also known as quantum spin hall (QSH) insulator. It features odd number of Kramers pairs and gapless edge modes which conduct spin-up and spin-down electrons in the opposite direction – a hallmark of topological materials. These spin edge states are protected by the time-reversal symmetry and are robust against small perturbations and weak electron-electron interaction [81, 82]. The two phases are separated by a topological phase transition, which is triggered by the closing of the bulk bandgap at a critical point of the system’s parameters.

Topological phase transitions (TPT) are typically studied within the tight-binding (TB) approximation, which replaces the continuum Hamiltonian with a simplified discrete model. This approach describes hopping between localized electronic orbitals bounded to the atomic sites and generally provides accurate solutions for the low-energy part of the spectrum. This has made convenient to analytically investigate TPTs in crystals including flat bands lattices such as Kagome, Lieb and decorated honeycombs [83–87]. A few approaches based on TB models have been proposed to generate flat band lattices [88, 89], with graph theory often playing a prominent role in such studies [90–92]. Along these lines, Mielke demonstrated ferromagnetism in linegraphs of a bipartite lattice [93, 94]. Recently, many 2D flat band systems have been systematically constructed from simple bipartite lattices (such as honey-

comb or square lattice) serving as the root graph, and by using graph theoretical tools such as line and split graph operations to generate new structures [90, 91]. These graphs usually exhibit topologically trivial flat bands, spanned by the combination of localized states associated with flat bands and delocalized states from dispersive bands [95] that touch at a high-symmetry point of the Brillouin zone. These dispersionless bands are protected by the material point group symmetries, making them tunable via symmetry-breaking perturbations. Further, by introducing SOC the degenerate flat bands transform into isolated quasi-flat bands, obtain nontrivial topology and become QSH insulators.

In this paper, we utilize unifying graph theoretic tools to systematically generate a variety of complex 2D Euclidean lattices with flat bands from bipartite parent (root) graphs. The number of times line and split graph operations applied to the parent graph determines the generation number. For instance, first-generation lattices are obtained directly as line and split graphs of the parent, while second-generation lattices include structures like the line graph of a split graph. These generations inherit all the lattice symmetries and band structure features of their predecessors, such as flat bands with quadratic and Dirac band crossings, and isolated Dirac cones, while adding additional bands of similar characteristics. Consequently, our study focuses till second-generation graphs, as they encompass all possible combinations of these band structures. While some the structures studied here are very well studied in the literature (e.g. Kagome lattice), many others presented here are understudied (e.g. triangular Kagome), while some are new (e.g. checkerboard splitgraph).

We investigate, at the TB level, the role of system's parameters such as inter-atomic hopping amplitude, SOC, on-site potential and strain on TPT. Strain, alters bond lengths and angles, can effectively change the band structure and provide fine control over quantum phases. Strain engineering has been of particular interest in material science to tune the electronic, magnetic and topological properties of materials [96, 97]. Additionally, in some cases external strain (e.g. through substrates) has been shown crucial in imparting thermodynamical stability to low dimensional materials [98–101]. Here, we analyze the effect of strain on the topological features of energy bands of various lattices generated through our graph-theoretic framework. Although our attention is largely on states close to the Fermi level, we also discuss electronic bands away from the Fermi level, since these can be rele-

vant in many experimental scenarios. Such bands can be accessed through methods such as electrostatic gating, non-equilibrium photo-excitation, electro-chemical doping, Floquet engineering, and nonlinear optical experiments.

The rest of the paper is organized as follows. In section II, we will give an overview of graph theoretic tools used to generate various 2D lattices, the tight binding model as well as the topological and electronic phases observed in these structures. Section III presents the results, touching on topological and quantum phase transitions observed in first and second generation of root (parent) graph due external perturbations like strain. We conclude in section IV.

II. PRELIMINARIES

In this section, we give a general introduction to the graph theoretic results and tools used to generate different structures from primitive bipartite lattices. More details can be found in standard textbooks on graph theory and in papers [90, 91, 102, 103]. We also briefly introduce the tight-binding model used to investigate electronic and topological properties of lattices. First, we layout the notation used in the rest of the paper.

In what follows, the lattice $\mathcal{L} \subset \mathbb{R}^2$ is the discrete group of translations which contains the set of periodically arranged lattice points \mathcal{P} . We will consider \mathcal{L} as a d -regular Euclidean lattice with $d \geq 3$, where d is the coordination number. The lattice vectors will be denoted as $\mathbf{a}_1 = a[1, 0]$ and $\mathbf{a}_2 = a[\cos \theta, \sin \theta]$, where $\theta = \frac{\pi}{2}$ and $\theta = \frac{\pi}{3}$ for the structures with square and hexagonal geometries, respectively, and a is the lattice constant for all structures considered here (which we set equal to 1). The vector of Pauli matrices is $\boldsymbol{\sigma} = \{\sigma_x, \sigma_y, \sigma_z\}$ which will denote the spin space, for the orbital space $\boldsymbol{\tau}$ and $\boldsymbol{\gamma}$ will be used with identity matrices σ_0, τ_0 and γ_0 . We will denote the standard orthonormal basis of \mathbb{R}^3 as $\mathbf{e}_1, \mathbf{e}_2, \mathbf{e}_3$. The matrices S_{ij} defined as $\mathbf{e}_i \otimes \mathbf{e}_j$ are also used to construct tight binding Hamiltonian in orbital space.

A. Graphs theoretic tools and tight binding model

For each lattice \mathcal{L} we will associate a graph $\mathcal{X} = (\mathcal{V}, \mathcal{E})$, where the set $\mathcal{V}(\mathcal{X})$ contains exactly one vertex related to each of the lattice points in \mathcal{P} and $\mathcal{E}(\mathcal{X})$ is the set containing the edges connecting the nearest neighbor. If \mathcal{X} is bipartite, then $\mathcal{V}(\mathcal{X})$ can be decomposed into two disjoint and independent sets X and Y such that every edge in $\mathcal{E}(\mathcal{X})$ always connects a vertex in X to a vertex in Y . The prototypical examples of this in Euclidean lattices are square and hexagonal honeycomb lattices; we will refer to them as parent (root) graph lattices \mathcal{X} , where blue and red color atoms can be considered in sets X and Y , respectively (illustrated in the first column of Fig. 1).

A line graph $L(\mathcal{X})$ can be formed by placing a vertex $v_i \in \mathcal{V}(L(\mathcal{X}))$ at the midpoint of an edge $e_i \in \mathcal{E}(\mathcal{X})$ and connecting vertices v_i and v_j for adjacent edges e_i and e_j in \mathcal{X} . The new vertices are the new atomic sites and equal to the set of edges of \mathcal{X} , $\mathcal{V}(L(\mathcal{X})) = \mathcal{E}(\mathcal{X})$. For example, the line graph of square and honeycomb lattice are checkerboard and kagome lattice, respectively, shown in the second column of schematic in Fig. 1a & 1c. The split graph $S(\mathcal{X})$ is generated by adding an extra vertex on each edge $e_i \in \mathcal{E}(\mathcal{X})$, as depicted as Lieb and honeycomb-kagome lattices in Fig. 1a & 1c. We call these graphs the first generation of \mathcal{X} . Further generations can simply be build by the application of line- and split-graph operations on the previous generation. These subsequent lattices inherit all periodic and symmetric properties of their respective parent graphs, such as all square and hexagonal lattices possess four fold (C_4) and six fold (C_6) rotational symmetry. In this paper, we will restrict ourselves till second generation graphs shown in third column Fig. 1.

The physics of fermionic motion on the 2D graph lattices, generated from the line graph and split graph operations, can be simply described using the single-orbital per site tight binding (TB) method. The general TB Hamiltonian $H_{\mathcal{X}}$ is given by,

$$H_{\mathcal{X}} = \sum_{i,\sigma} \varepsilon_i c_{i,\sigma}^\dagger c_{i,\sigma} + \sum_{\langle i,j \rangle, \sigma} t_{ij} c_{i,\sigma}^\dagger c_{j,\sigma} + i\lambda_I \sum_{\langle\langle i,j \rangle\rangle, \alpha\beta} c_{i,\alpha}^\dagger (\mathbf{e}_{ij} \cdot \boldsymbol{\sigma})_{\alpha\beta} c_{j,\beta} + \text{H.c.}, \quad (1)$$

where, ε_i is the onsite energy of vertex v_i , $c_{i,\sigma}^\dagger$ and $c_{j,\sigma}$ are the fermionic creation and annihilation operators with spin $\sigma \in \{\uparrow, \downarrow\}$, t_{ij} is the hopping amplitude between adjacent vertices v_i and v_j , $\langle i, j \rangle$ and $\langle\langle i, j \rangle\rangle$ are the nearest-neighbor (NN) and next nearest neighbor (NNN)

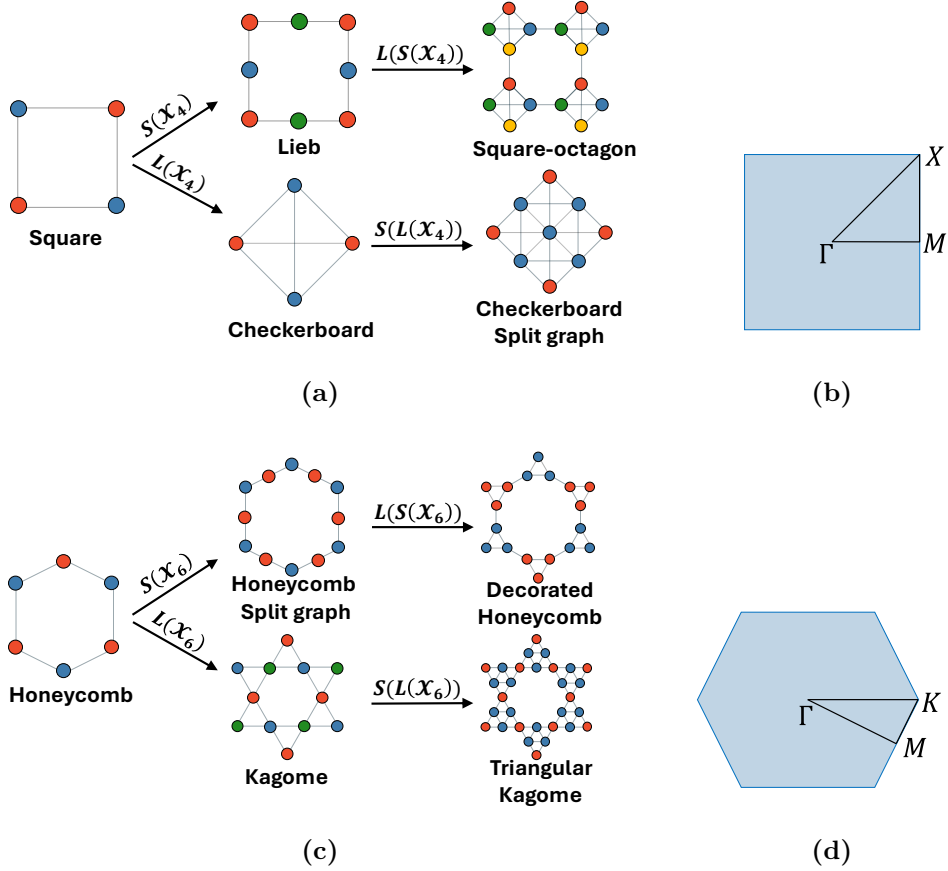


FIG. 1: Schematic showing the application of split graph and line graph operations to generate different type of lattices from bipartite lattice, square \mathcal{X}_4 and honeycomb \mathcal{X}_6 . (a) Starting from the parent (root) bipartite square lattice \mathcal{X}_4 , the splitgraph $S(\mathcal{X}_4)$ operation gives a commonly known Lieb lattice and linegraph $L(\mathcal{X}_4)$ gives checkerboard lattice (second column). Further applying linegraph function on Lieb lattice gives square-octagon lattice $L(S(\mathcal{X}_4))$ and splitgraph of checkerboard lattice gives $S(L(\mathcal{X}_4))$. (b) First Brillouin zone of the square lattices, where Γ , M and X denotes the symmetry points (c) Applying similar procedure, honeycomb-kagome $S(\mathcal{X}_6)$, kagome $L(\mathcal{X}_6)$, decorated honeycomb $L(S(\mathcal{X}_6))$ and triangular kagome $S(L(\mathcal{X}_6))$ can be obtained from the parent honeycomb lattice. (d) First Brillouin zone of the hexagonal lattices, where Γ , M and K denotes the symmetry points.

pairs, respectively. The third term describes the intrinsic spin-orbit coupling (SOC) between the NNN sites whose relative position is described by the unit vector $\mathbf{e}_{ij} = \frac{\mathbf{d}_{kj}^1 \times \mathbf{d}_{ik}^2}{|\mathbf{d}_{kj}^1 \times \mathbf{d}_{ik}^2|}$, where the bond vector \mathbf{d}_{kj}^1 points from the vertex v_j to the nearest vertex v_k and the second bond vector \mathbf{d}_{ik}^2 directs from the vertex v_k to the closest vertex v_i . Here, α and β denote the fermionic spin as σ and λ_I is the intrinsic SOC parameter. The intrinsic SOC preserves the s_z spin-symmetry but it can uplift the degeneracy between the bands, driving the system into a quantum spin Hall state[76]. The SOC interaction will be considered between the second nearest neighbor throughout the paper, unless mentioned otherwise.

Exploiting the translation symmetry of the 2D lattices, the total Hamiltonian in the momentum space is diagonalized as $H = \sum_{\mathbf{k}\sigma} \Psi_{\mathbf{k}\sigma}^\dagger \tilde{H}_{\mathbf{k}\sigma} \Psi_{\mathbf{k}\sigma}$, where $\Psi_{\mathbf{k}\sigma}^\dagger = (c_{1\mathbf{k}\sigma}^\dagger, c_{2\mathbf{k}\sigma}^\dagger, \dots, c_{n\mathbf{k}\sigma}^\dagger)$ is the basis representing the number of sites in the unit cell, $\tilde{H}_{\mathbf{k}\sigma}$ is the Hamiltonian in the Fourier or reciprocal space. Here, \mathbf{k} is restricted to the fundamental domain in reciprocal space, known as the first 2D Brillouin zone (BZ) shown in Fig. 1d & 1b.

For every d -regular Euclidean lattice with equal hopping amplitude t_{ij} between adjacent vertices, there exists a one-to-one correspondence with any mathematical graph \mathcal{X} . This implies that the hopping Hamiltonian (second term in eq. 1) can also be expressed in terms of the adjacency (transition) operator of the \mathcal{X} :

$$H_{TB} = tA_{\mathcal{X}}. \quad (2)$$

Here, $A_{\mathcal{X}} = MM^\dagger - D_{\mathcal{X}}$, where $D_{\mathcal{X}}$ is the coordination matrix and has a form $D_{\mathcal{X}} = d\mathbb{I}_m$. M is $m \times n$ incidence operator of parent graph \mathcal{X} with m and n are the number of vertices and edges, respectively. The entries of M are 1 when edges and vertices are incident, otherwise 0. Since the graph considered here are periodic, we exploit the Bloch theorem to write M in momentum space. For example, for the bipartite honeycomb graph (\mathcal{X}_6) $D_{\mathcal{X}_6} = 3\mathbb{I}_2$ and M is 2×3 matrix as its unitcell has 2 independent vertices and 3 edges. The line graph, $L(\mathcal{X})$, is a $2d - 2 > 3$ regular Euclidean lattice and satisfies the relation $M^\dagger M = A_{L(\mathcal{X})} + 2\mathbb{I}_m$. The split graph $S(\mathcal{X})$ is a $d, 2$ -biregular graph then its line graph $L(S(\mathcal{X}))$ is also d -regular Euclidean graph (also known as Hoffman graphs). The adjacency operators for both the

types of graph can be written in terms of incidence matrix of parent graph:

$$\begin{aligned}
 A_{S(\mathcal{X})} &= \begin{pmatrix} 0 & M \\ M^\dagger & 0 \end{pmatrix}, \\
 A_{L(S(\mathcal{X}))} &= \begin{pmatrix} M(\frac{M^\dagger+N^\dagger}{2}) - \mathbb{I}_m & \mathcal{D} \\ \mathcal{D}^\dagger & M(\frac{M^\dagger+N^\dagger}{2}) - \mathbb{I}_m \end{pmatrix}.
 \end{aligned} \tag{3}$$

Above, \mathbb{I}_l is the $l \times l$ identity operator, \mathcal{D} is the diagonal matrix of \mathcal{X} in momentum space and N is $m \times n$ directed incidence matrix of parent graph \mathcal{X} :

$$N_{ij} = \begin{cases} 1, & \text{if } e_j \text{ enters } v_i, \\ -1, & \text{if } e_j \text{ leaves } v_i, \\ 0 & \text{otherwise.} \end{cases} \tag{4}$$

From the above relations and with given spectrum $E_{\mathcal{X}}(\mathbf{k})$ of parent graph, we can determine the spectrum of Hamiltonian of $L(\mathcal{X})$, $S(\mathcal{X})$ and $L(S(\mathcal{X}))$ in the reciprocal space, denoted as $E_{L(\mathcal{X})}$, $E_{S(\mathcal{X})}$ and $E_{L(S(\mathcal{X}))}$, respectively. Using the results stated in ref. [102], the eigenenergies of these graphs follow the relations:

$$\begin{aligned}
 E_{L(\mathcal{X})}(\mathbf{k}) &= \{2\}^\infty \cup \{d - 2 + E_{\mathcal{X}}(\mathbf{k})\} \\
 E_{S(\mathcal{X})}(\mathbf{k}) &= \begin{cases} \pm \sqrt{E_{\mathcal{X}}(\mathbf{k}) + d} \\ 0, \end{cases} \\
 E_{L(S(\mathcal{X}))}(\mathbf{k}) &= \begin{cases} 2, \\ \frac{1 \pm \sqrt{1 + 4(E_{\mathcal{X}}(\mathbf{k}) + d)}}{2}, \\ 0. \end{cases}
 \end{aligned} \tag{5}$$

The eigenvalues 2 and 0 have infinite multiplicity and give rise to flat bands consisting of localized eigenstate with compact support, arising from the destructive interference of hopping amplitudes[95]. Since \mathcal{X} is a bipartite lattice, these flat bands are gapless with the dispersive bands touching at high symmetry quasi-momentum point. By introducing SOC the gap can be opened, thus inducing \mathbb{Z}_2 topology. The dispersion-less bands can be naturally gapped [90, 104] if and only if \mathcal{X} non-bipartite graphs. Additionally, the gapped flat bands in non-bipartite lattices can exhibit fragile topology without SOC [20, 104, 105].

B. Modeling strain and topological phase diagram

The realization of materials with equal hopping amplitude and zero on-site energy is very special, belonging to highly symmetric class. The realistic materials with lattice geometries in Fig. 1 can deviate from the ideal graph theoretic spectrum due to their specific chemical characteristics such as orbital hybridization (related to hopping parameter) and different on-site energies. In this paper, we use different values of hopping parameter, on-site energy, SOC and deformation that will take band structures far from the ideal graph theory spectrum. Different on-site energies and deformations break various lattice symmetries, distort symmetry protected eigenstates which can lead to fascinating quantum phase transitions. For example, flat band with quadratic band touching evolve into tilted Dirac cones when the six fold symmetry of the Kagome lattice is broken [55, 83, 84, 106–109]. The strain changes the bond lengths and it can be incorporated by applying the displacement field $\mathbf{u}(\mathbf{r}) = (u_x(\mathbf{r}), u_y(\mathbf{r}))$, where \mathbf{r} is an atomic position vector. The new lattice sites after deformation are at $\mathbf{r}' = \mathbf{r} + \mathbf{u}(\mathbf{r})$. For uniform strain, the displacement field can be written as $\mathbf{u}(\mathbf{r}) = \hat{\epsilon} \cdot \mathbf{r}$. Here $\hat{\epsilon}$ is the strain tensor:

$$\hat{\epsilon} = \epsilon \begin{pmatrix} \cos^2 \varphi - \nu \sin^2 \varphi & (1 + \nu) \cos \varphi \sin \varphi \\ (1 + \nu) \cos \varphi \sin \varphi & \sin^2 \varphi - \nu \cos^2 \varphi \end{pmatrix}. \quad (6)$$

Here, ν is the Poisson's ratio, ϵ is the strain magnitude and φ is the direction of applied strain with respect to the x -axis. The vectors joining the adjacent vertices transform as $\tilde{\mathbf{d}}_{ij} = (\mathbb{I}_2 + \hat{\epsilon}) \cdot \mathbf{d}_{ij}$. The hopping amplitude, which depends on the edge length, changes according to:

$$\tilde{t}_{ij} = t_{ij} \exp \left[-\beta \left(\frac{|\tilde{\mathbf{d}}_{ij}|}{|\mathbf{d}_{ij}|} - 1 \right) \right], \quad (7)$$

where, i and j denoted the vertices and β is the Grüneisen parameter. For the purpose of the paper, β is set to 3 and ν is equal to 0.165 [110]. These parameters are well known for the graphene material, but, as for most of the lattices considered here, the corresponding values have not yet been reported, so we choose the same values.

On introducing intrinsic SOC, the gap between the bulk energy bands can open up, and the topologically protected helical states manifest at the edges of quasi-1D nanoribbon. To

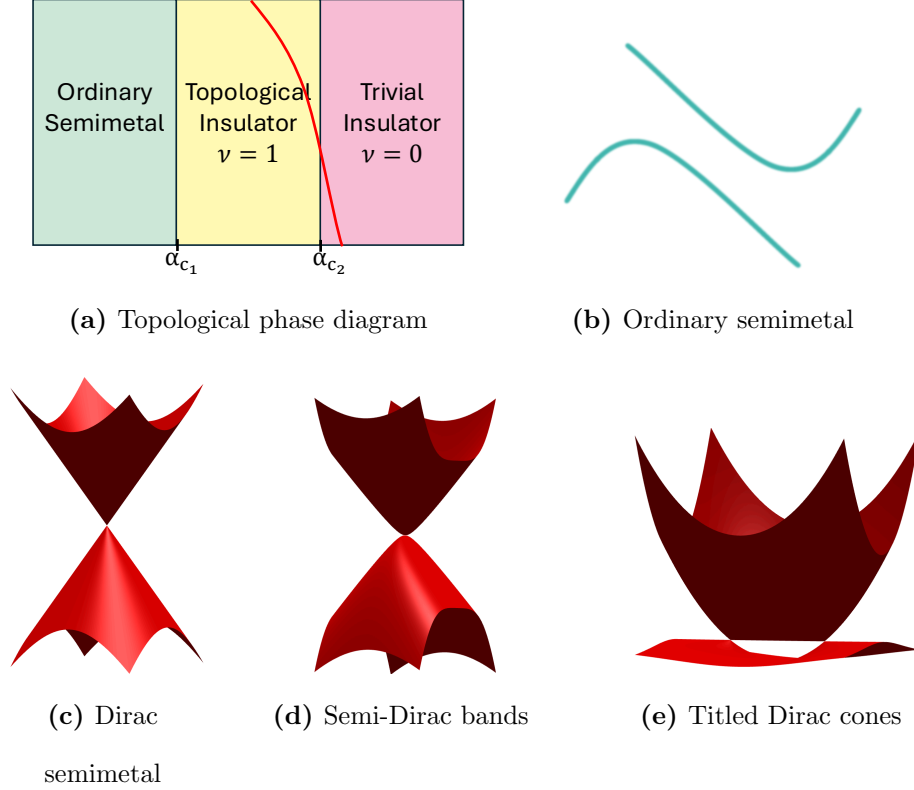


FIG. 2: (a) Schematic of a phase diagram in parametric space showing phases that can appear in different lattices generated using line graph $L(\mathcal{X})$ and split $S(\mathcal{X})$ graph operations. The red line denotes the Dirac semimetallic state, ν is the \mathbb{Z}_2 index, and α_{c_1} α_{c_2} are the critical points (strain or system parameters) where the bandgap vanishes. Note that not all lattices show the phases highlighted here, and the order of appearance of the phases can also be different from the depiction above. Illustration of (b) ordinary semimetal, (c) Dirac semimetal, (d) semi-Dirac bands and (e) tilted Dirac cones.

visualize the edge states, we considered our model on the nanoribbons and calculated the 1D spectrum which clearly reveals the bands crossing the bulk gap. The topological state of the system can also be characterized by the topological index \mathbb{Z}_2 , denoted as ν , which can be obtained by tracking the evolution of Wannier charge centers using Z2pack [111, 112]. When $\nu = 1$, the lattice supports the topological edge states in the bulk gap, whereas, at $\nu = 0$, the lattice will be a trivial insulator.

Apart from this, the 2D lattices can exhibit diverse electronic phases, such as 2D Dirac (Weyl) semimetal (DSM), semi and tilted Dirac bands, and semi ordinary semimetal (OSM). The DSM phase is associated with massless relativistic fermions, where the conduction and valence bands touches locally in the conical manner with energy dispersion $E_{\pm}(k) \propto \pm|k|$, where k is quasi-momentum parameter (Fig. 2c). These bands carry a Berry (winding) phase of $\pm\pi$ that keeps the Dirac nodes locally stable [113–115]. The semi-Dirac bands features hybrid dispersion, being linear in one direction and quadratic in other, as represented in Fig. 2d. On the other hand, the tilted Dirac bands shown in Fig. 2e consist of a tilted cone characterized by massless fermions, accompanied by directional flat bands where electrons have very high effective mass. Finally, in te OSM phase, the valence and the conduction bands cross the Fermi level without overlapping each other, maintaining distinct energies across all quasi-momentum space as illustrated in Fig. 2b.

The filling fraction denotes how many bands are fully occupied in the system. Tuning the magnitude and direction of the applied strain along with the system parameters (such as hopping amplitudes, on-site energies, and intrinsic SOC), the material can undergo TPT at different filling fractions. Specifically, we observed 2D (Dirac) semimetallic [116], topological nontrivial ($\nu = 1$) or trivial ($\nu = 0$) phases (not all lattices show all phases and also in the same order) in the lattices as illustrated by a phase diagram shown in Fig. 2. In the next section, we analyzed the effect of strain along with system’s parameters on the band structure and and topological phases in periodic graphs.

III. RESULTS

In this section, we discuss the effect of strain and system parameters on electronic and topological properties of lattices shown in Fig. 1. We start with the root graphs — square and honeycomb lattices — where the effect of deformation on quantum properties is negligible owing to the simplicity of the lattice. Then we discuss first generation lattices, i.e., split graphs (Lieb and honeycomb split graph lattices) and line graphs (checkerboard and kagome lattices). In the end, we focus on second generation lattices, namely line of split graph (square-octagon, decorated honeycomb) and split graph of line graphs (split graph of

checkerboard and triangular-kagome).

A. Parent Graphs

As seen in the section II, the Euclidean parent (root) graphs form the foundation of many complex topological and flat-band systems. The simplest example is a square lattice (\mathcal{X}_4), formed by all integer linear combinations of two linearly independent vectors in \mathbb{R}^2 , shown in Fig. 3a. The explicit form of TB Hamiltonian of \mathcal{X}_4 containing one atom in the unit cell is:

$$H_{\mathcal{X}_4}(\mathbf{k}) = -2t(\cos \mathbf{k} \cdot \mathbf{a}_1 + \cos \mathbf{k} \cdot \mathbf{a}_2). \quad (8)$$

The band structure plotted in Fig. 3b exhibit the cosine-like dependence on the momentum

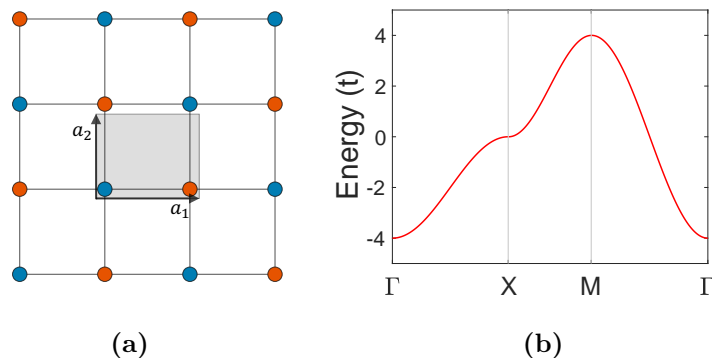


FIG. 3: (a) The schematic of bipartite square lattice, \mathcal{X}_4 . The black arrows indicate the lattice vectors \mathbf{a}_1 and \mathbf{a}_2 , and the gray region is the unit cell. (b) Tight-binding band diagram without SOC.

space. At half-filling, the lattice has a gapless metallic phase with saddle point at X -point in BZ with associated van-Hove singularity in the density of states. Due to its simplicity and features, square lattice has become a playground for exploring exotic phenomena such as magnetism and unconventional superconductivity [117–119].

A parent graph for hexagonal lattices is a honeycomb lattice, which is the periodic translations of two points (sublattices) in two dimensions (Fig. 4a). This atomic arrangement renders honeycomb lattice an unique electronic properties characterized by massless Dirac

fermions at the K -points where the conduction and valence bands meet linearly (see the red band diagram in Fig. 4b). The spinful Hamiltonian with SOC in Fourier space is given as:

$$\begin{aligned}
 H_{\mathcal{X}_6} = & \left(1 + \sum_{i=1}^3 t_i \cos \mathbf{k} \cdot \mathbf{a}_i \right) \tau_x \otimes \sigma_0 + \left(\sum_{i=1}^3 t_i \sin \mathbf{k} \cdot \mathbf{a}_i \right) \tau_y \otimes \sigma_0 \\
 & + \lambda_I \left(\sum_{i=1}^3 (-1)^{i+1} \sin \mathbf{k} \cdot \mathbf{a}_i \right) \tau_z \otimes \sigma_z \quad (9)
 \end{aligned}$$

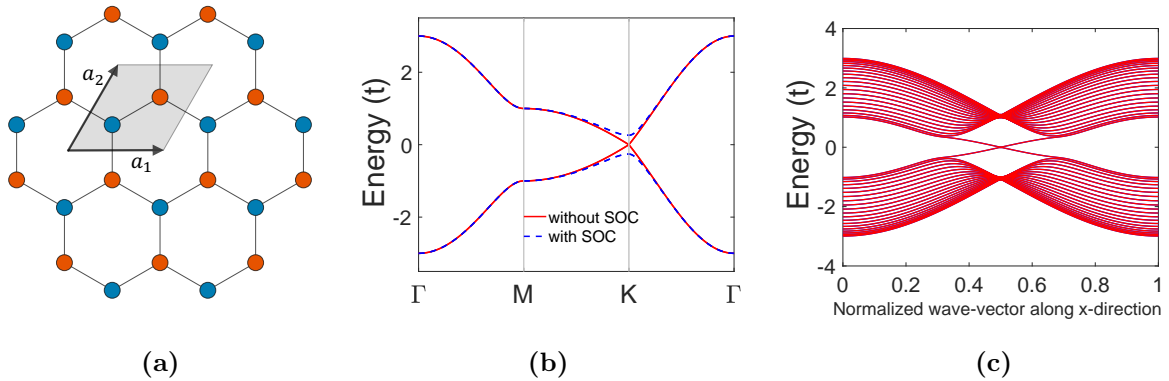


FIG. 4: (a) The schematic of bipartite honeycomb lattice, \mathcal{X}_6 . The black arrows indicate the lattice vectors \mathbf{a}_1 and \mathbf{a}_2 , and the gray region is the unit cell. The tight binding band diagrams of (b) 2D lattice without (red solid line) and with (blue broken line) SOC ($\lambda_I = 0.1t$), and (c) 1D zigzag hexagonal honeycomb nanoribbon with $\lambda_I = 0.1t$.

In the absence of SOC, the TB Hamiltonian of honeycomb lattice exhibits an electronic band structure of pristine graphene. It is a widely studied material of fundamental importance and interest[7]. Here, C_3 symmetry on top of inversion and time reversal symmetries induced global stability to the Dirac nodes by making them fixed at K -points and gapless. Breaking the C_3 symmetry by applying strain moves the Dirac cones away from the K -points but it remains gapless for small strain. Under high anisotropic limit (high strain), the band structure becomes gapped [120] without inducing topological character. The nonzero SOC parameter can trigger gapless edge states in the quasi-1D nanoribbons with gapped bulk bands (broken blue lines in Fig. 4b) and nontrivial \mathbb{Z}_2 index as shown in Fig. 4c.

For the purpose of the paper we considered strain up till the reasonable limit of 10%. Under this limit these two simple lattices do not show any significant change in the topological characteristics (graphene is shown to have TPTs under very high anisotropic limits [116]). The subsequent generations of parent graphs show fascinating quantum phase transitions, which we systematically study below.

B. First generation graphs

The first generation lattices comprises total of four lattices formed by split graph, $\mathcal{S}(\mathcal{X})$, and line graph, $L(\mathcal{X})$ operations on both the parent lattices.

1. Split graphs $\mathcal{S}(\mathcal{X})$

The split graphs are $d, 2$ -biregular Euclidean lattices where additional sites are placed at the edge center of parent graphs. The energy spectrum of these structures, given by eq. 5, are particle-hole symmetric and consist of a flat band at zero energy which touches dispersive bands at the Dirac point forming a threefold degenerate point [91]. Near the point of degeneracy, the low energy Hamiltonian of these three set of bands can be described by the 3×3 matrices that form spin-1 representation of SU(2). This is in higher angular momentum than the spin-1/2 Pauli matrices representation of Dirac cones in hexagonal honeycomb lattice [121, 122].

The well-known split graph is the Lieb lattice in square geometry [87] as shown in Fig. 5a. The explicit form of spinful TB Hamiltonian of Lieb lattice, $S(\mathcal{X}_4)$ is:

$$H_{S(\mathcal{X}_4)}(\mathbf{k}) = \sum_{i=1}^3 \varepsilon_i S_{ii} \otimes \sigma_o + \left(\sum_{i=1}^2 t_i (1 + \cos \mathbf{k} \cdot \mathbf{a}_i) \Lambda_i - \sum_{i=4}^5 t_{i-3} \sin \mathbf{k} \cdot \mathbf{a}_{i-3} \Lambda_i \right) \otimes \sigma_o - \lambda_I (1 - e^{i\mathbf{k} \cdot \mathbf{a}_1} - e^{i\mathbf{k} \cdot \mathbf{a}_2} + e^{i\mathbf{k} \cdot (\mathbf{a}_2 - \mathbf{a}_1)}) \Lambda_3 \otimes \sigma_z, \quad (10)$$

where, S_i is defined as $\mathbf{e}_i \otimes \mathbf{e}_i$ and matrices Λ_i are Gell-Mann matrices defining the orbital space (see appendix A). In the pristine system, with equal on-site energies, without SOC and strain, the band structure is represented by the solid red lines in Fig. 5b, where the flat band lies in between of two linearly dispersive bands. This non-dispersive band is

degenerate with the Dirac bands at the M -point in the square BZ. With inclusion of SOC, the bands become isolated with a gap of $\Delta = 4|\lambda_I|$ at Dirac point (shown by broken blue lines in Fig. 5b). Additionally, the flat band transforms into topological non-trivial state with corresponding counter-propagating spins represented in the quasi-1D ribbon band diagram (Fig. 5c).

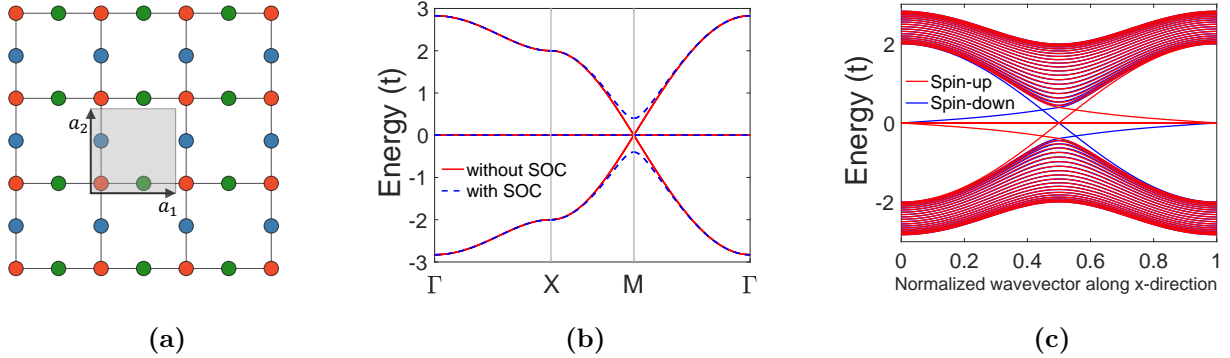


FIG. 5: (a) The schematic of split graph of bipartite square graph (Lieb lattice, $S(\mathcal{X}_4)$). The black arrows indicate the lattice vectors \mathbf{a}_1 and \mathbf{a}_2 , and the gray region is the unit cell. The tight binding band diagram of (b) 2D lattice without (red solid line) and with (blue broken line) SOC ($\lambda_I = 0.1t$) and (c) 1D zigzag Lieb lattice nanoribbon at $\lambda_I = 0.1t$. The red and blue lines show the counter-propagating spin-up and spin-down states, respectively.

The triple degeneracy at the M -point is protected by the rotational symmetries of the pristine lattice. Several translational symmetry preserving perturbations and different on-site energies breaks the rotational symmetry. This can influence the stability of flat band and can introduce additional features to the band structure. Within the NN TB model, the flatband does not show any distortion on application of strain [106, 107]. Interestingly, a non-zero on-site energy (ε_b) at the green atom transforms the upper Dirac and flat bands into two tilted Dirac cones (D, D') (see Fig. 6b) with opposite winding number ($+1, -1$). The lower Dirac cone emerges into a semi-Dirac band, linear in one direction and quadratic in the other, which touches the middle band at M -point (Fig. 6b). On further increasing the on-site potential, the D and D' Dirac points approach toward each other starting from M and M' points, respectively, as shown in Fig. 6c. When $\varepsilon_b = 2$, Dirac points merge into a

semi-Dirac band at X with total winding number zero and the top band become directionally flat (Fig. 6d). At $\varepsilon_b > 2$ the gap opens up between the middle and top band but the bottom band never get isolated. The evolution of top two bands can be simply captured by the generalized Hamiltonian in the vicinity of the X -point [108]:

$$\mathcal{H}(\mathbf{k}) = \left(\delta + \frac{k_x^2}{2m} \right) \tau_a + ck_y \tau_b, \quad (11)$$

where, τ_a can be τ_x or τ_z , τ_b is τ_y , and δ , m and c are the parameters. Here, δ plays the role of ε_b . The tilted Dirac cone phase corresponds to $\delta < 0$, at $\delta = 0$ it transform to semi-Dirac band and finally the gap opens when $\delta > 0$. An uniform strain combined with site asymmetry

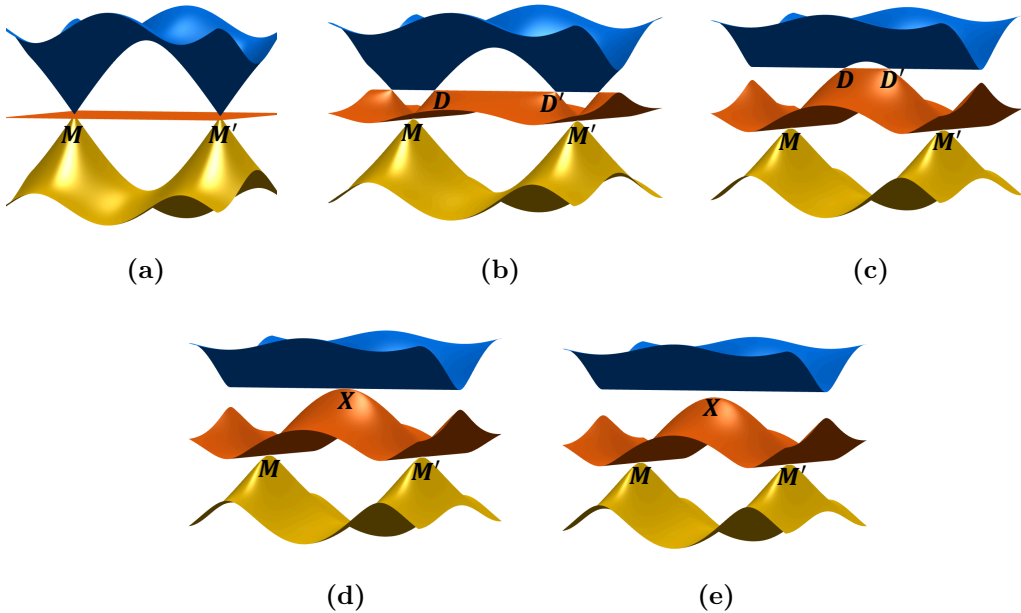


FIG. 6: Emergence and motion of two pairs of tilted Dirac cones (D, D') at (M, M') points in Brillouin zone in the top band from triply degenerate point when on-site potential ε_b is varied (a) $\varepsilon_b = 0$, (b) $\varepsilon_b = 0.8$, (c) $\varepsilon_b = 1.8$, (d) $\varepsilon_b = 2$ and (e) $\varepsilon_b = 2.2$. At $\varepsilon_b = 2$, the tilted Dirac cones with opposite winding numbers ($+1, -1$) merges to form semi-Dirac band at point X with zero winding number, shown in (d) and when $\varepsilon_b > 2$ the top two bands become gapped as shown in (e).

generates intriguing topological phase diagrams. At filling fraction $2/3$, with fixed intrinsic SOC parameter, we observed that varying the strain along x-direction (ε_{xx}) and the on-site

energy (ε_b), results in linear phase boundary between the trivial and topological phases. A prototypical example is shown in Fig. 7 where for $\lambda_I = 0.2t$, increasing ε_{xx} from -10% to 10% the phase boundary vary linearly between $\varepsilon_b = 1.9$ and $\varepsilon_b = 2.1$. In other words, at $\varepsilon_b = 2$, the uniaxial distortion drives the flat band in Lieb lattice from trivial phase to topological phase. Additionally, varying the orientation with magnitude of applied strain

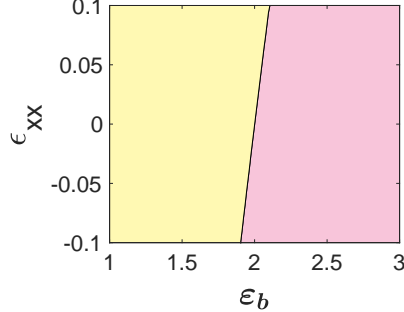


FIG. 7: Topological phase diagram of Lieb lattice at $2/3$ filling as the function of strain in x -direction (ε_{xx}) and on-site energy (ε_b) at $\lambda_I = 0.2t$. The phases are distinguished by the colors as follows. Yellow (□): topological band insulator and pink (□): band insulator.

also influences the system's phases. A notable effect occurs near the transition point $\varepsilon_b = 2$, where middle band undergoes transition from the tilted Dirac cones to gaped phase passing through semi-Dirac band phase. The phase diagrams in the $\varepsilon - \varphi$ space in Fig. 8 show that at $\varepsilon_b = 1.9$ the majority region is the topological phase except the at top right pink region when the strain is positive the middle band become trivial band insulator (Fig. 8a). In contrast, at $\varepsilon_b = 2.1$, the central band majorly exhibits trivial phase except the area under compressive strain as represented in Fig. 8c. At the transition point, $\varepsilon_b = 2$, there are equal diagonal and antidiagonal patches of topological and trivial phases, shown in Fig. 8b.

In the hexagonal graphs \mathcal{X}_6 , the split graph $\mathcal{S}(\mathcal{X}_6)$ is referred to as Honeycomb-Kagome (HK) lattice as it combines structural and electronic features of both of Honeycomb and Kagome lattices[123, 124]. Specifically, the unit cell consists of five atoms: the red sites, shown in Fig. 9a forms a Kagome lattice, while the blue atoms occupy the corners. The spinful TB Hamiltonian for this structure can be expressed as:

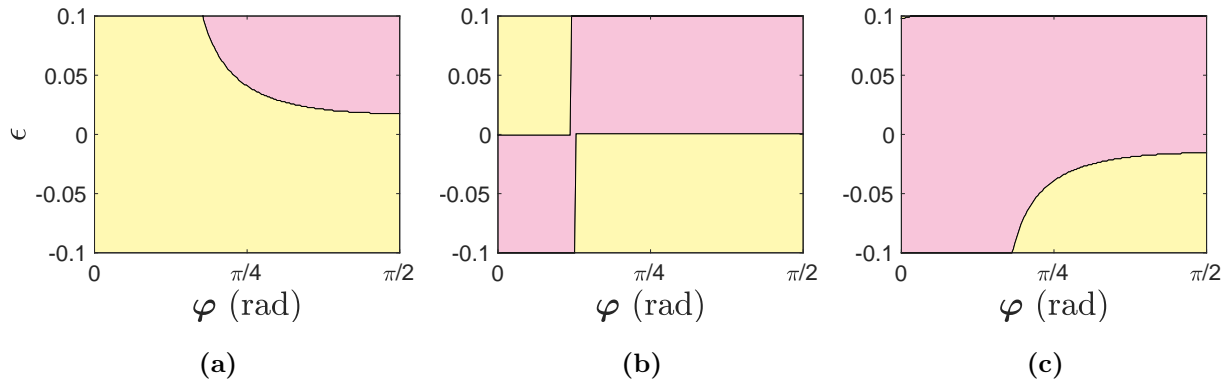


FIG. 8: Topological phase diagram of Lieb lattice at 2/3 filling as the function of magnitude ϵ and the direction φ of applied strain for on-site energy (a) $\epsilon_b = 1.9$, (b) $\epsilon_b = 2$ and (c) $\epsilon_b = 2.1$.

The phases are distinguished by the colors as follows. Yellow (): topological band insulator and pink (): band insulator.

$$H_{S(\mathcal{X}_6)}(\mathbf{k}) = H_{S(\mathcal{X}_6)}^O(\mathbf{k}) \otimes \sigma_0 + H_{S(\mathcal{X}_6)}^{SO}(\mathbf{k}) \otimes \sigma_z, \quad (12)$$

where,

$$H_{S(\mathcal{X}_6)}^O(\mathbf{k}) = \begin{pmatrix} \mathcal{O}_{2 \times 2} & \Phi^\dagger(\mathbf{k}) \\ \Phi(\mathbf{k}) & \mathcal{O}_{3 \times 3} \end{pmatrix}, \quad \text{with } \Phi(\mathbf{k}) = \begin{pmatrix} t & t \\ t & te^{-i\mathbf{k} \cdot \mathbf{a}_1} \\ t & te^{-i\mathbf{k} \cdot \mathbf{a}_2} \end{pmatrix}, \quad (13)$$

and

$$H_{S(\mathcal{X}_6)}^{SO}(\mathbf{k}) = \lambda_I \left(\tau_0 \oplus \left(\sum_{j=1}^3 (-1)^j \sin \mathbf{k} \cdot \mathbf{a}_j \Lambda_j - \sum_{j=4}^6 (1 + \cos \mathbf{k} \cdot \mathbf{a}_{j-3}) \Lambda_j \right) \right) \quad (14)$$

The TB band diagram is drawn in Fig. 9b, is symmetric about zero energy and contains a flat band which is triply degenerate with the linearly dispersive band at the Γ point. The non-zero λ_I isolates all the bands represented by broken blue lines in Fig. 9b and the system becomes non-trivial with edge states, which can be visualized in Fig. 9c. The magnitude of the gap between flat band and the Dirac band is given by $\Delta = 2\sqrt{3}|\lambda_I|$. Similar to the Lieb lattice, the flat band in HK lattice also remains dispersionless under deformation within the NN TB model. However, in absence of SOC, we observed an external strain opens up a gap between the both the Dirac cones at K point without introducing topological character. Site

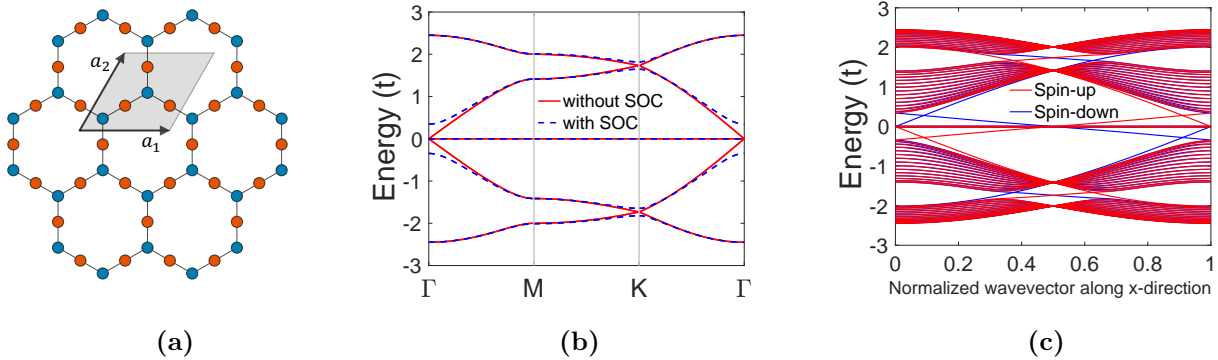


FIG. 9: (a) The splitgraph of honeycomb lattice $S(\mathcal{K}_6)$. The black arrows indicate the lattice vectors \mathbf{a}_1 and \mathbf{a}_2 , and the gray region is the unit cell. The tight binding band diagram of (b) 2D lattice without (red solid line) and with (blue broken line) SOC ($\lambda_I = 0.1t$) and (c) 1D zigzag lattice nanoribbon with $\lambda_I = 0.1t$. The red and blue lines show the counter-propagating spin-up and spin-down states, respectively.

asymmetry in HK lattice also produces fascinating effects to the electronic and topological properties. First, we focus on its effect on electronic structure (Fig. 10). Introducing a non-zero on-site energy (ε_c) at one of the red atoms splits the upper linearly dispersive and flat band into tilted Dirac spectrum near the Γ point whereas the lower Dirac band (at $2/5$ filling) converts into semi-Dirac state, as shown in Fig. 10a. Unlike in the Lieb lattice, increasing ε_c causes the separation between the titled Dirac cones widen but they never merge with Dirac nodes entering from neighboring BZ. Intriguingly, at $\varepsilon_c = 1.05$ and $4/5$ filling fraction, the Dirac points at K and K' with opposite winding numbers $\{1, -1\}$ annihilate into semi-Dirac bands, as represented in Fig.10c. When $\varepsilon_c > 1.05$, the the fifth band become isolated (see Fig. 10d). Fig. 11 and Fig. 12 presents some noteworthy topological phase diagrams at a filling fraction of $4/5$, illustrating how the phases varies as the function of magnitude of uniaxial deformation (ε_{xx}) with it's orientation (φ) and on-site energy (ε_c). When $\lambda_I = 0.4t$, the phase boundary shifts linearly as both ε_{xx} and ε_c are increased (Fig.11a). The $\lambda_I = 0.4t$ can also be particularly interesting because the middle three bands transforms into isolated non-dispersive bands at equal onsite energies. Further, increasing the SOC to $\lambda_I = 0.6t$ in Fig. 11b, the boundary shifts to higher value of ε_c and also becomes non-linear at higher

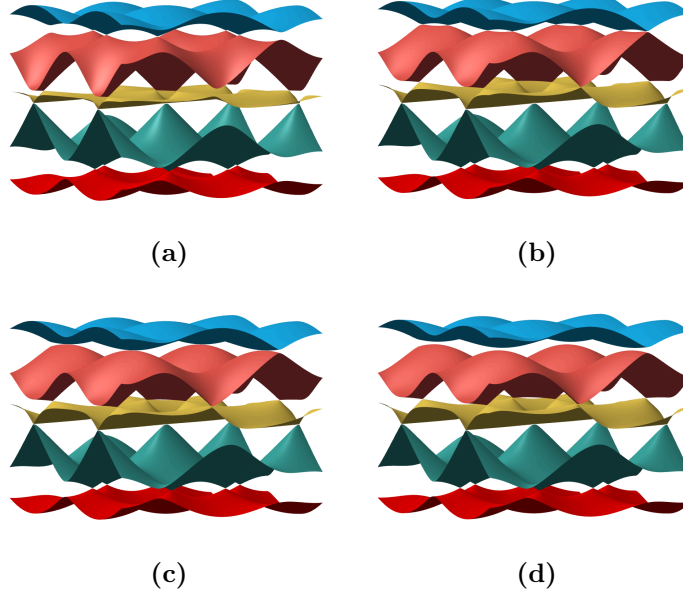


FIG. 10: Evolution of Dirac cones of opposite winding numbers at $4/9$ filling fraction starting from K and K' points when on-site potential ε_c is varied. (a) $\varepsilon_c = 0.5t$ (b) $\varepsilon_c = 0.9t$ (c) $\varepsilon_c = 1.05t$ (d) $\varepsilon_c = 1.1t$. The Dirac cones merges at $\varepsilon_c = 1.05t$ and form semi-Dirac cones and finally separates at $\varepsilon_c = 1.1t$

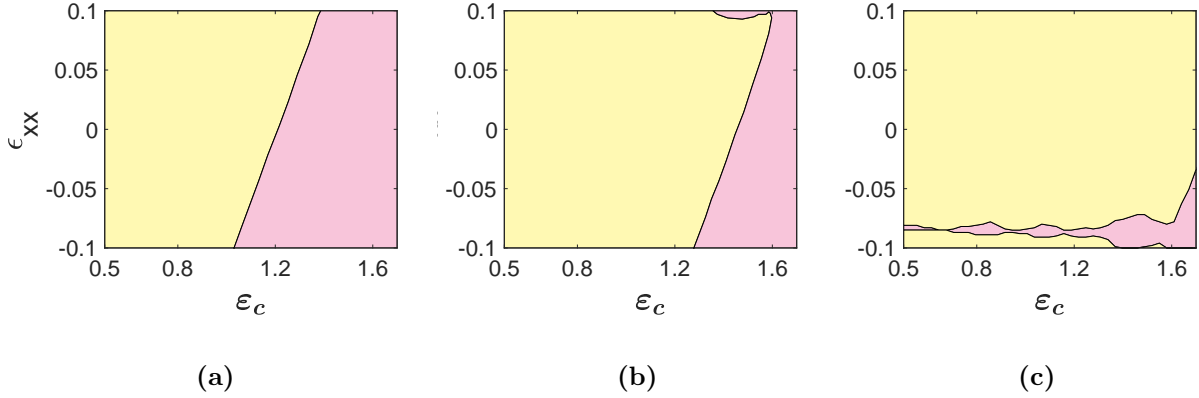


FIG. 11: Topological phase diagram of honeycomb splitgraph lattice at $4/5$ filling as the function of strain in x-direction (ε_{xx}) and on-site potential (ε_c) at (a) $\lambda_I = 0.4t$ (b) $\lambda_I = 0.6t$ and (c) $\lambda_I = 0.8t$. The different phases are distinguished by the colors as follows. Cyan (\square): semimetal, yellow (\square): topological band insulator and pink (\square): band insulator.

strain. The phase boundary become completely non-trivial at $\lambda = 0.8t$, where trivial phase only appear at the compressive strain, as shown in 11c.

In HK lattice as well, altering the angle of the applied strain also influences the gap closing points. Interestingly, at the transition point $\varepsilon_c = 1.05$, the phase boundary is parallel to x-axis, showing no dependence on the magnitude of the strain (Fig. 12b). However, in the vicinity of $\varepsilon_c = 2$, the separation between the two phases changes its curvature from concave downwards in Fig. 12a ($\varepsilon_c = 1$) to convex shape in Fig. 12c ($\varepsilon_c = 1.1$).

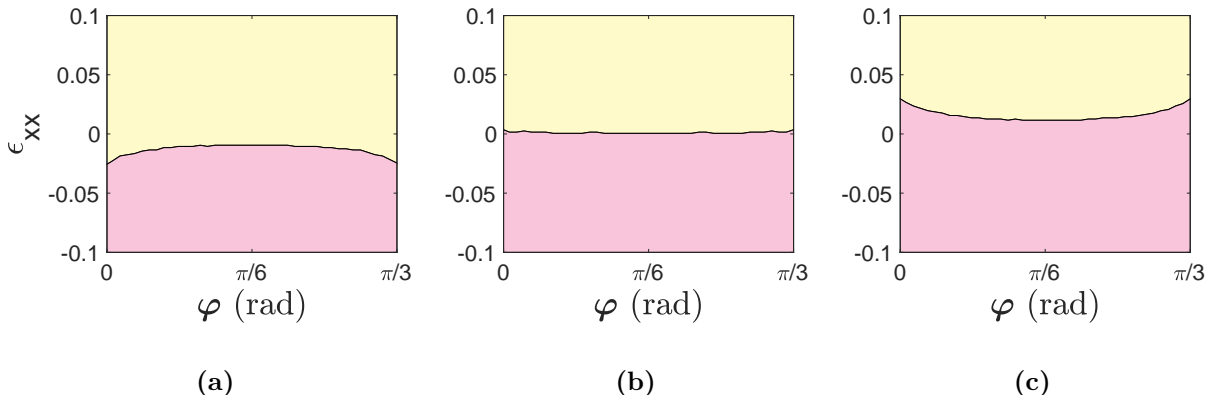


FIG. 12: Topological phase diagram of honeycomb splitgraph lattice at 4/5 filling as the function of strain in x-direction (ε_{xx}) and on-site potential (ε_c) at $\lambda_I = 0.2t$ and (a) $\varepsilon = 1$ (b) $\varepsilon = 1.05$ and (c) $\varepsilon = 1.10$. The different phases are distinguished by the colors as follows. Yellow (): topological band insulator and pink (): trivial band insulator.

2. Line graphs $\mathcal{L}(\mathcal{X})$

The line graphs of the parent lattices have been a playground for understanding strongly correlated and topological properties of flat band materials. The coordination number of these graphs is given by $2d - 2$, and they are commonly known as the checkerboard ($\mathcal{L}(\mathcal{X}_4)$) and Kagome lattice ($\mathcal{L}(\mathcal{X}_6)$), as depicted in Fig. 13a and Fig. 14a, respectively. Here, for completeness, we will briefly review the each lattice. The energy spectrum of these lattices, given by the first equation in 5, has a flat band at $E = 2$ which touches a dispersive band

parabolically. The touching point is stabilized by the C_4 and C_6 rotational symmetry of the checkerboard and Kagome unit cell, respectively. The low-energy Hamiltonian at this point can be written as [83, 84, 109]:

$$\mathcal{H}(\mathbf{k}) = (k_x^2 + k_y^2)\mathbb{I} + 2k_x k_y \tau_x + (k_x^2 - k_y^2)\tau_z. \quad (15)$$

Any symmetry breaking perturbations such as distortion either creates gap between these two bands or convert the quadratic touching point into tilted Dirac bands. The isolated bands in the above Hamiltonian can generated by adding $m\tau_x$, whereas tilted Dirac cones appears due to $m\tau_z$ term. Here, m is known as mass.

The checkerboard lattice is a bipartite lattice with two atoms in the unit cell, as illustrated in Fig. 13a. Due to its structural simplicity, it is usually employed as the toy model in the studies of fractional quantum hall effect [27, 125, 126]. The four-bands spinful Hamiltonian can be written as:

$$H_{L(\chi_4)} = \left(\frac{t_1}{2}(1 + \tau_z) \cos \mathbf{k} \cdot \mathbf{a}_1 + \frac{t_1}{2}(1 - \tau_z) \cos \mathbf{k} \cdot \mathbf{a}_2 \right) \otimes \sigma_o + \left(\left(1 + \sum_{i=1}^3 \cos \mathbf{k} \cdot \mathbf{a}_i \right) \tau_x + \left(\sum_{i=1}^3 (-1)^i \sin \mathbf{k} \cdot \mathbf{a}_i \right) \tau_y \right) \otimes (t_2 \sigma_o + i\lambda_I \sigma_z). \quad (16)$$

Here, t_1 and t_2 are the hopping amplitude between the same and different atomic species, respectively. When t_1 and t_2 are equal, the spectrum contains a flat band across the entire BZ with quadratic band touching at M -point. The dispersive band here is reminiscent of square lattice spectrum. The band structure, in this case, is shown by red lines in Fig. 13b. In contrast, when $t_1 \neq t_2$ directional flat band appears from X to M point. With non-zero λ_I , the bands become isolated and the flat band transform into a quasi-flatband as represented by broken blue lines. The dispersion graph of checkerboard ribbon is drawn in Fig. 13c at $\lambda_I = 0.2t_1$, where non-trivial edge states emerge in quasi-1D structure. Given its simplicity, we have not found any significant strain-induced effects on its topological properties.

The Kagome lattice consists of three sublattices arranged in pattern of corner sharing triangles, as shown in Fig. 14a. The explicit form TB Hamiltonian of Kagome lattice with spin degree of freedom reads

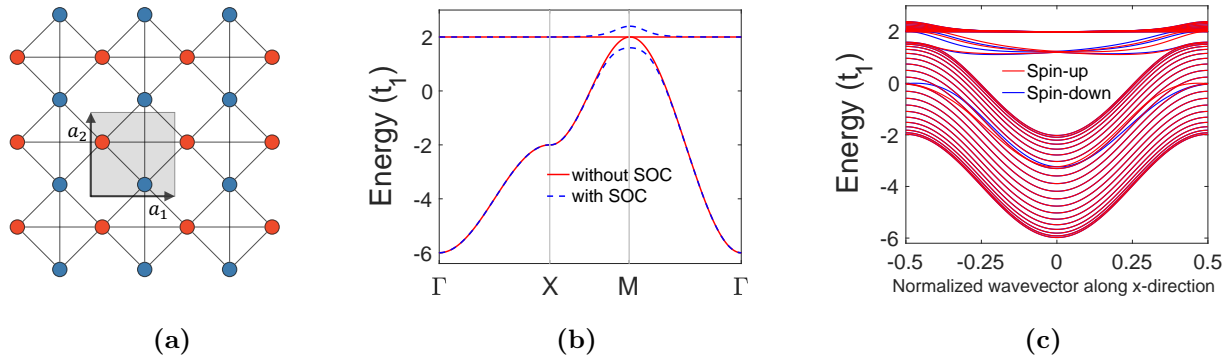


FIG. 13: (a) The line graph of the square lattice (Checkerboard lattice $L(\mathcal{X}_4)$). The black arrows indicate the lattice vectors \mathbf{a}_1 and \mathbf{a}_2 , and the gray region is the unit cell. The tight binding band diagram of (b) 2D lattice without (red solid line) and with (blue broken line) SOC ($\lambda_I = 0.1t_1$) and (c) 1D zigzag lattice nanoribbon with $\lambda_I = 0.1t_1$. The red and blue lines show the counter-propagating spin-up and spin-down states, respectively.

$$\begin{aligned}
H_{S(\mathcal{X}_4)}(\mathbf{k}) = & \sum_{i=1}^3 \varepsilon_i S_i \otimes \sigma_o + \left(\sum_{i=1}^3 t_i (1 + \cos \mathbf{k} \cdot \mathbf{a}_i) \Lambda_i - \sum_{i=4}^6 t_{i-3} \sin \mathbf{k} \cdot \mathbf{a}_{i-3} \Lambda_i \right) \otimes \sigma_o \\
& + \lambda_I \left(\sum_{i=4}^6 (\cos \mathbf{k} \cdot \mathbf{a}_{i+2} + \cos \mathbf{k} \cdot \mathbf{a}_{i+1}) \Lambda_i + \sum_{i=1}^3 ((-1)^i \sin \mathbf{k} \cdot \mathbf{a}_{i+2} \right. \\
& \left. + \sin \mathbf{k} \cdot \mathbf{a}_{i+1}) \Lambda_i \right) \otimes \sigma_z,
\end{aligned} \tag{17}$$

In the spectrum of Kagome lattice dispersionless and Dirac bands - inherited from honeycomb lattice - coexists, as depicted by the red lines in Fig. 14b. The flat band touches the Dirac band quadratically at the Γ -point at $E = 2$. With SOC, the gap opens up between all three bands with a magnitude of $\Delta = 4\sqrt{3}|\lambda_I|$ and the system turns topological. The flat band also become slightly dispersive, as represented by broken blue line in Fig. 14b. The corresponding quasi-1D Kagome nanostrip band diagram at $\lambda_I = 0.2t$ is shown in Fig. 14c, which clearly reveals helical edge states crossing the gap at $1/3$ and $2/3$ fillings.

The coexistence of these two types of paradoxical bands makes the Kagome lattice as one of the most intriguing lattice models, showcasing a range of emerging fundamental physical phenomena such as superconductivity, fractional quantum hall effect, quantum spin liquid

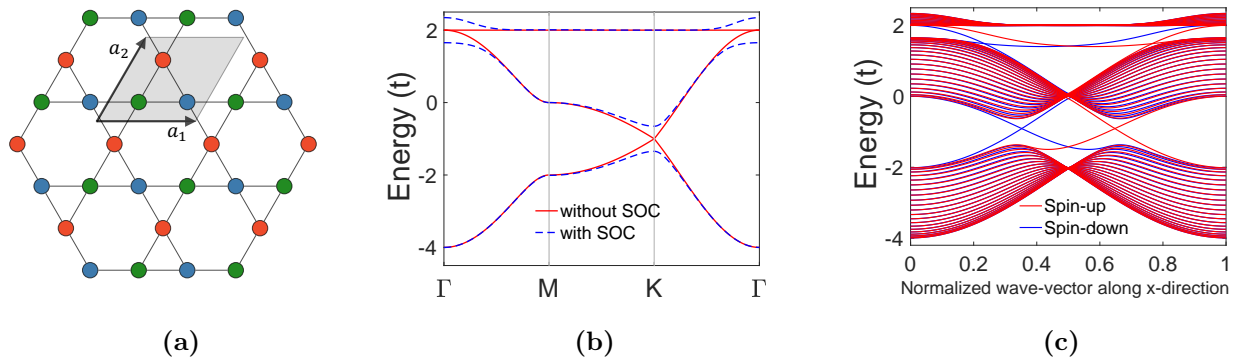


FIG. 14: (a) The line graph of honeycomb lattice $L(\mathcal{X}_6)$ also known as Kagome lattice. The black arrows indicate the lattice vectors \mathbf{a}_1 and \mathbf{a}_2 , and the gray region is the unit cell. The tight binding band diagram of (b) 2D lattice without (red solid line) and with (blue broken line) SOC ($\lambda_I = 0.1t$) and (c) 1D zigzag lattice nanoribbon with $\lambda_I = 0.1t$. The red and blue lines show the counter-propagating spin-up and spin-down states, respectively.

and topological phases. The effect of strain on the electronic and topological properties of the Kagome lattice has been rigorously studied. We guide the reader to these papers [83, 84, 109, 127]. Additionally, the structural and electronic properties of line graph of hexagonal graph (Kagome lattice) and split graph of square lattice (Lieb lattice) are interconvertible into each other by applying strain in the diagonal direction [107].

C. Second generation lattices

Second generation lattices are generated by applying a combination of split and line graph operations twice to the parent graph. Here, we analyzed line of split graphs $L(S(\mathcal{X}))$ and split of line graph $S(L(\mathcal{X}))$. For each configuration, we construct two distinctive structures based on 4-regular square and 3-regular hexagonal cases. These lattices inherit many of the electronic and topological features from their precursors. However, due to bigger unit cell and more system parameters to tune, the phase diagrams of second generation lattices are richer than structures considered earlier.

1. *Line graph of split graph $L(\mathcal{S}(\mathcal{X}))$*

Such graphs are realized by starting from the d -regular parent graphs \mathcal{X} then take the $d, 2$ -biregular graph $\mathcal{S}(\mathcal{X})$ and finally apply line graph operation to get $L(\mathcal{S}(\mathcal{X}))$ which is also d -regular. The schematic of $L(\mathcal{S}(\mathcal{X}))$ lattices, namely square-octagon lattice and decorated honeycomb lattice, are illustrated in Fig. 15a and Fig. 18a, respectively. Both lattices can be regarded as an interpolating structures between their respective parent graph \mathcal{X} and line graph $L(\mathcal{X})$. For instance, in the case of the square lattice (\mathcal{X}_4), the square plaquettes at the vertices can be progressively shrunk to their central points, eventually recovering the original square lattice. Conversely, expanding the square plaquettes until their corners touch transforms the structure into the checkerboard lattice, $L(\mathcal{X}_4)$.

The spectrum of these graphs the is given by last equation in 5. They possess gapless flat bands at $E = 0$ and $E = 2$ touches the dispersive band parabolically and additional bands which are inherited from their respective predecessors. Here, the quadratic band touching point is also protected by lattice's rotational symmetry and follows the same description around equation 15.

First, we analyze the line graph of checkerboard lattice, $L(S(\mathcal{X}_4))$, which gives square-octagon lattice. The basic building block of the lattice is a square plaquette consisting of four atoms, as illustrated in Fig. 15a. Recently, the lattice has attracted significant attention due to plethora of novel phases predicted in this system such as quantum magnetic phases[128], topological insulating phases [129–131] and high-temperature superconductivity states [132]. The spinful single-orbital per site TB Hamiltonian of square-octagon lattice takes a form:

$$\begin{aligned}
 H_{L(S(\mathcal{X}_4))}(\mathbf{k}) = & \left(t_1(\Gamma_{01} + \Gamma_{11}) + \frac{1}{2}((t_3 + t_2 \cos \mathbf{k} \cdot \mathbf{a}_1)(\Gamma_{10} + \Gamma_{13}) + (t_3 + t_2 \cos \mathbf{k} \cdot \mathbf{a}_2)(\Gamma_{10} - \Gamma_{13})) \right. \\
 & \left. - \sin \mathbf{k} \cdot \mathbf{a}_1(\Gamma_{20} + \Gamma_{23}) + \sin \mathbf{k} \cdot \mathbf{a}_2(\Gamma_{20} - \Gamma_{23}) \right) \otimes \sigma_0 \\
 & + i\lambda_I((e^{i\mathbf{k} \cdot \mathbf{a}_1} + \cos \mathbf{k} \cdot \mathbf{a}_2)(\Gamma_{12} - \Gamma_{02}) - i \sin \mathbf{k} \cdot \mathbf{a}_2 \Gamma_{12}) \otimes \sigma_z, \quad (18)
 \end{aligned}$$

where, the matrices Γ_{ij} defined as $\tau_i \otimes \gamma_j$, and the hopping parameters: t_1 is along the sides of square, t_2 is between the two adjacent squares and t_3 is hopping amplitude connecting the diagonals of the squares. As discussed earlier, the band structure of $L(S(\mathcal{X}_4))$ in the ideal isotropic case ($t_1 = t_2 = t_3$) contains a couple of flat bands at $E = 0$ and $E = 2$

and dispersive bands. One of the dispersive bands is sandwiched between the two flat bands, touching quadratically the lower and upper flat band at M and Γ point, respectively (Fig. 15b). The other dispersive band at 1/4 filling, resembles that of parent square lattice (\mathcal{X}_4), is separated from the $E = 0$ flat band by the gap of $\Delta = 2t_1$.

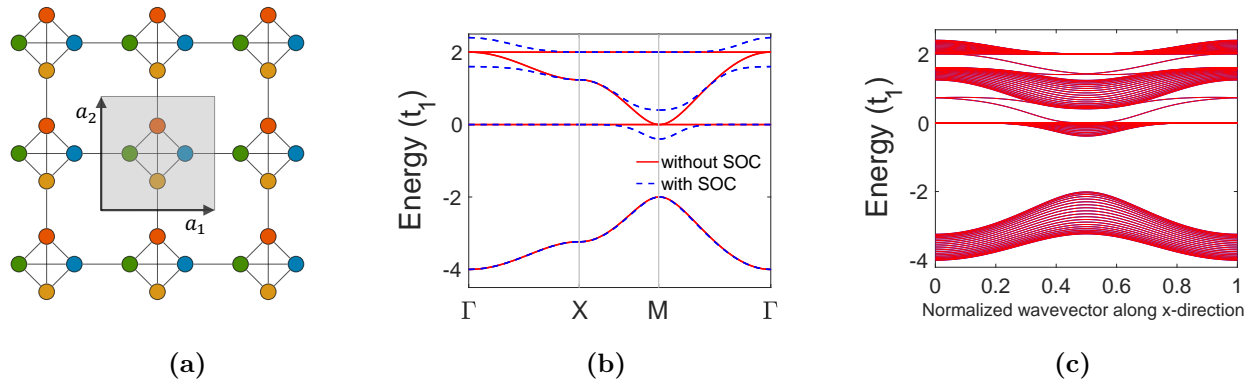


FIG. 15: (a) The line graph of the Lieb lattice gives square octagon lattice, $L(S(\mathcal{X}_4))$. The black arrows indicate the lattice vectors \mathbf{a}_1 and \mathbf{a}_2 , and the gray region is the unit cell. The tight binding band diagram of (b) 2D lattice without (red solid line) and with (blue broken line) SOC ($\lambda_I = 0.1t$) at $t_1 = t_2 = t_3$ and (c) 1D zigzag lattice nanoribbon with $\lambda_I = 0.1t$. The red and blue lines show the counter-propagating spin-up and spin-down states, respectively.

The inclusion of the diagonal hopping along with isotropic hopping energies is critical for generating a flat band across the whole BZ. Interestingly, when $t_3 \neq t_1$, the band structure features various emerging quantum phases, including Lieb lattice like pseudospin-1 Dirac cones with directional flat bands. The cases when $t_3 < t_1$ are particularly intriguing (Fig. 16). At $t_3 = 0.62t_1$, the third and fourth band become flat and degenerate along the entire $\Gamma - X$ while the second band is dispersionless from $X - M$ with a parabolic touching with the third band at M (Fig. 16a). As t_3 decreases further, the third band become directionally dispersionless, as shown in Fig. 16b. Finally, when $t_3 = 0$, the band structure become chiral symmetric as the triply degenerate Dirac band crossing at the Γ point also appear at the M point (Fig. 16c). In this limiting case, the Hamiltonian satisfies the symmetry relation $H_{L(S(\mathcal{X}_4))}[k_x + \pi, k_y + \pi] = -H_{L(S(\mathcal{X}_4))}[k_x, k_y]$. A mathematical analysis of the low energy

expressions of band structures in the two limits are given in [133–135].

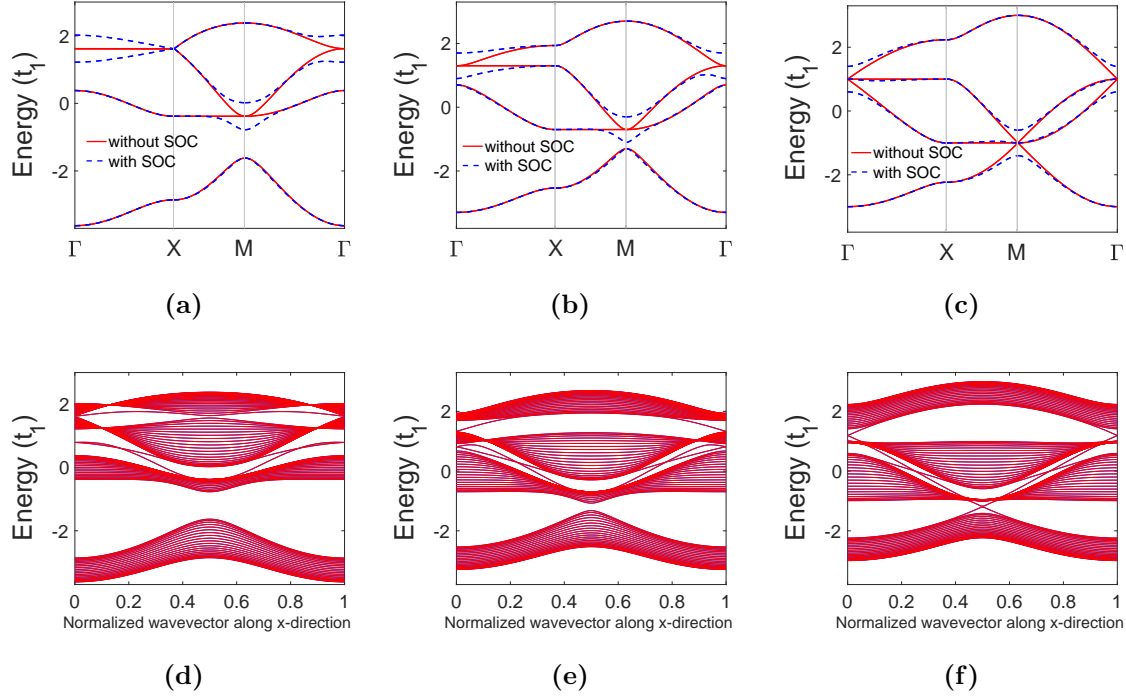


FIG. 16: Evolution of diagonal connection square-octagon to no interaction between the diagonals. The 2D band diagrams with (rid lines) and without SOC (broken blue lines) at (a) $t_3 = 0.62t_1$, (b) $t_3 = 0.3t_1$ and (c) $t_3 = 0$. (d) to (f) Corresponding quasi-1D band ribbon band diagrams. The spin orbit coupling parameter is $\lambda_I = 0.1t$.

The gap between the degenerate bands open up at $\lambda_I = 0.1t_1$, as represented by dashed blue lines in Figs. 15b and 16a to 16c. In the isotropic limit, the lattice at 1/2 and 3/4 filling fraction show QSH state while the first band remains trivial insulator. Fig. 15c shows the spectrum of square-octagon strip geometry where the helical edge states can be observed at time-reversal invariant momentum 0 and π at 1/2 and 3/4 filling fraction, respectively. On decreasing t_3 , we observed that the second band transforms into semimetallic state and at $t_3 = 0$ the edge states appear only in the lowest band and third band, as depicted in Figs. 16d to 16f.

Interestingly, square octagon lattice exhibits three distinct quantum phases at 1/4 filling in the strain-SOC space for different values of t_2 with $t_3 = 0$, as shown in Figs. 17a to 17c.

The phase boundaries vary linearly with the strain. In the pristine case ($\epsilon_x x = 0$), SOC open up energy gap of value $\Delta = |4\lambda_I + 2t_2 - 2|$ ($t_1 = 1$), indicating that for $t_2 = 1$ the lower band is topological for any non-zero value of λ_I . However, under tensile strain, semimetallic phase emerges accompanied by the appearance of a trivial insulating phase at smaller values of λ_I , as represented in Fig. 17c.

To observe the topological phases, we calculated the ribbon band diagram. Figs. 17d to 17f show the behavior of edge modes at 1/4 filling and $t_2 = 0.5t_1$ through the transition between phases. The phase diagram at 3/4 filling is same due to chiral symmetry. In the trivial phase shown in Fig. 17d at uniaxial compression $\epsilon_{xx} = -0.1$ and $\lambda_I = -0.2$, there are no edge modes. However, as expected in the $\nu = 1$ phase, the edge states traverse in the bulk gap at the same strain and $\lambda_I = -0.7$ (see Fig. 17e). On increasing the strain, the edge protected modes have bulk conduction and valance bands merged into each other at the same value of λ_I , as depicted in Fig. 17f. Even in this case, we can observe that there are edge modes at the time reversal invariant point π and can be shown to be localized along the boundaries of the nanoribbon. However, they are they are not robust against the disorder and can mix with the bulk states, hence not “topologically protected”. The decorated Honeycomb lattice ($L(S(\mathcal{X}_6))$) can be obtained by applying line-graph operation on Honeycomb-Kagome lattice. Fig. 18a shows the unit cell of decorated honeycomb lattice containing six atoms arranged to form two equilateral triangle plaquettes symmetrically positioned with respect to the inversion center located at the center of the unit cell. The expression of spinful Hamiltonian is:

$$\begin{aligned}
H_{L(S(\mathcal{X}_6))}(\mathbf{k}) = & \left(\sum_{j=1}^3 t_j^1 \tau_0 \otimes \Lambda_j + \sum_{j=1}^3 t_j^2 (\cos \mathbf{k} \cdot \mathbf{a}_{j-1} \tau_x - \sin \mathbf{k} \cdot \mathbf{a}_{j-1} \tau_y) \otimes S_{jj} \right) \otimes \sigma_0 \\
& + \lambda_I \left(\left(1 + \sum_{j=4}^5 (-1)^{j-1} (\cos \mathbf{k} \cdot \mathbf{a}_{j-3} + i(-1)^j \sin \mathbf{k} \cdot \mathbf{a}_{j-3}) \right) \tau_x \otimes \Lambda_j \right. \\
& \left. + \sum_{j=1}^2 (-\cos \mathbf{k} \cdot \mathbf{a}_j + \sin \mathbf{k} \cdot \mathbf{a}_j) \tau_x \otimes \Lambda_6 \right) \sigma_z, \quad (19)
\end{aligned}$$

where, t_j^1 and t_j^2 denote the intra- and inter-triangular hopping amplitudes, respectively. The band structure, inherits in features from honeycomb and the kagome lattices, consists of two flat bands at $E = 0$ and $E = 2$ along with two sets of Dirac bands (Fig. 18b). In the

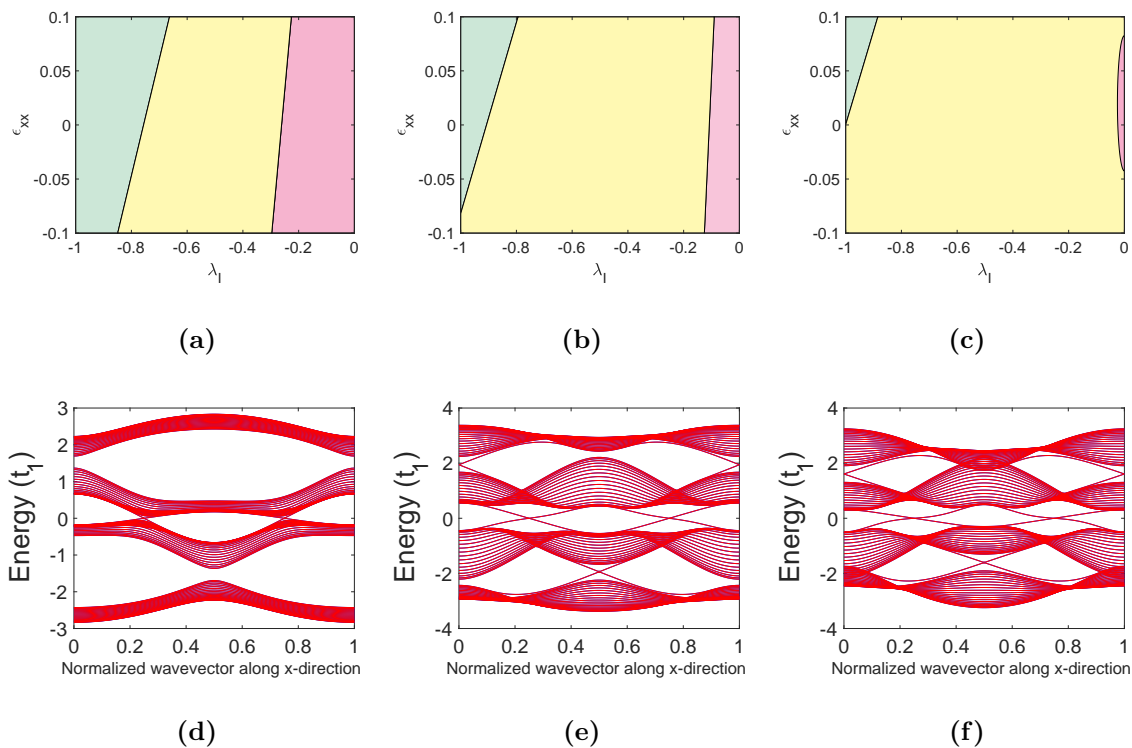


FIG. 17: Topological phase diagram of square octagon lattice at $1/4$ filling in uniaxial strain (ϵ_{xx}) and intrinsic SOC (λ_I) space with (a) $t_2 = 0.5t_1$ (b) $t_2 = 0.8t_1$ and (c) $t_2 = t_1$. The different phases are distinguished by the colors as follows. Cyan (\square): semimetal, yellow (\square): topological band insulator and pink (\square): band insulator. From (d) to (f) the square octagon nonribbon band diagrams at $t_2 = 0.5$ and (d) $\epsilon_{xx} = -0.1$, $\lambda_I = -0.2$, (e) $\epsilon_{xx} = -0.1$, $\lambda_I = -0.7$, and (e) $\epsilon_{xx} = 0.1$, $\lambda_I = -0.7$.

isotropic hopping parameter regime, one set of Dirac bands is sandwiched between the flat bands and exhibits quadratic band touching at the Γ -point, while the other set of Dirac bands remains isolated. Same as before, the states at Γ -point are not accidental and protected by the C_6 point group symmetry of the unit cell. At $t_j^2 = 1.5t_j^1$ for all j , the spectrum exhibits pseudospin-1 Dirac crossing at Γ -point like its immediate parent $\mathcal{S}(\mathcal{X}_6)$ graph. Due to its unique properties and capability to hold stable “realistic” carbon allotropes various studies has been performed including on 2D lattices [22, 136, 137] and quasi-1d materials such as nanotubes [55, 56].

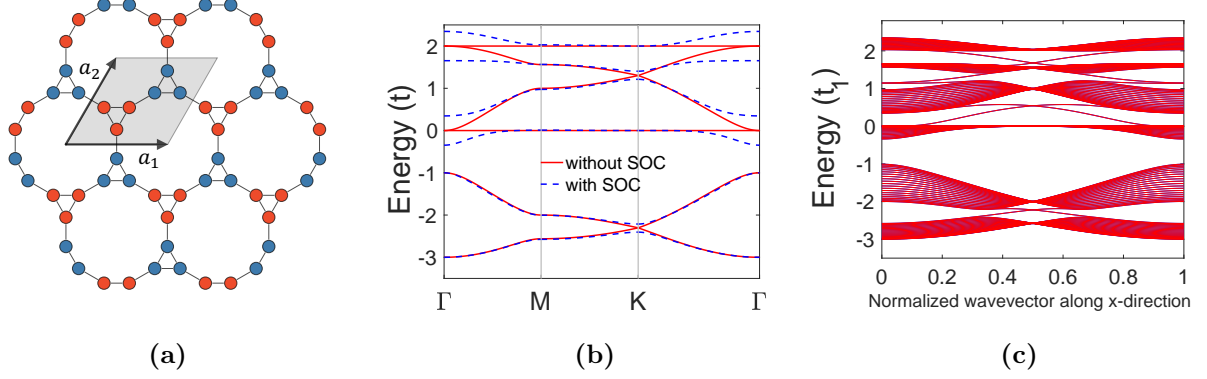


FIG. 18: (a) Line graph of honeycomb split graph $L(S(\mathcal{X}_6))$ also called as decorated honeycomb lattice. The black arrows indicate the lattice vectors \mathbf{a}_1 and \mathbf{a}_2 , and the gray region is the unit cell. The tight binding band diagram of (b) 2D lattice without (red solid line) and with (blue broken line) SOC ($\lambda_I = 0.1t$) and (c) 1D zigzag lattice nanoribbon with $\lambda_I = 0.1t$.

As usual, inclusion of SOC isolates the degenerate bands (blue dashed lines shown in Fig. 18b) and drives the system into QSH state at all the filling fraction. This is also evident from the spectrum of a decorated honeycomb nonribbon plotted in Fig. 18c, where the band crosses in the bulk gap at time reversal invariant momenta π and 0.

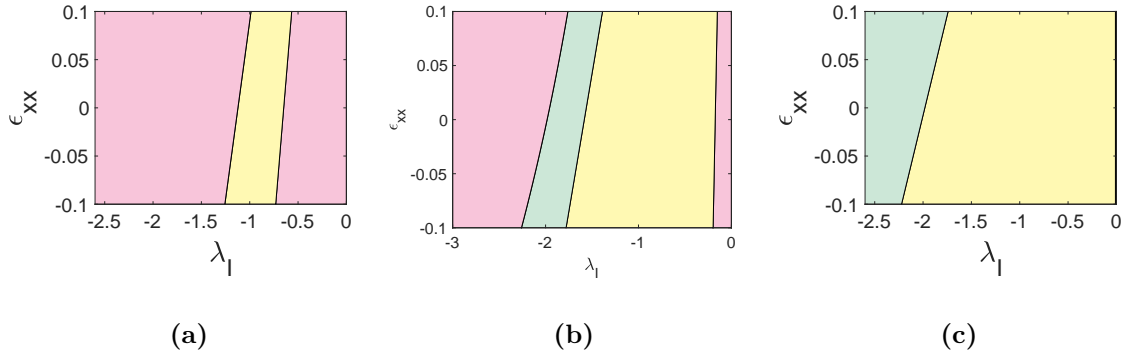


FIG. 19: Topological phase diagram of decorated honeycomb lattice, $L(S(\mathcal{X}_6))$, at $1/3$ filling as the function of strain (ϵ_{xx}) and intrinsic spin orbit coupling (λ_I) at (a) $t_2 = 0.4t^1$ (b) $t_2 = 1.2t^1$ and (c) $t_2 = 2.4t^1$. The different phases are distinguished by the colors as follows. Cyan (\square): semimetal, yellow (\square): topological band insulator and pink (\square): band insulator.

The lattice exhibit a rich variety of phases at different energy levels. Here, we highlight some of the most intriguing phase diagrams. Figures 19 and 20 show topological and quantum phases in strain-SOC space of the second Dirac band from bottom and of the flat band at $E = 0$, respectively, for different values of t_2 . At lower value of $t_2 < t_1$ trivial insulating phase dominates, with only narrow window of non-trivial state (Fig. 19a). While when $t_2 > t_1$, OSM phase emerges (Fig. 19b) and at $t_2 = 2.4t_1$ only semimetal and topological insulator phase persist (see Fig. 19c). In contrast, the flat band at $E=0$ behaves differently, as shown in Fig. 20. We observed that at $t_2 = 0.4t_1$ flat band transitions directly into the OSM phase from the non-trivial phase with a non-linear phase boundary. However, as t_2 increases, the OSM phase diminishes and the phase diagram becomes dominated by the trivial insulating phase, as illustrated in Figs. 20b and 20c.

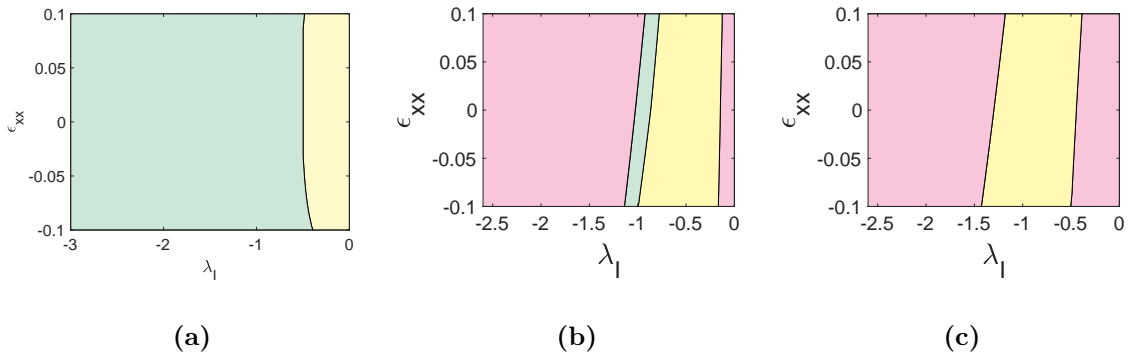


FIG. 20: Topological phase diagram of decorated honeycomb lattice, $L(S(\mathcal{X}_6))$, at 1/2 filling as the function of strain (ϵ_{xx}) and intrinsic spin orbit coupling (λ_I) at (a) $t_2 = 0.4t_1$ (b) $t_2 = 1.8t_1$ and (c) $t_2 = 2.4t_1$. The different phases are distinguished by the colors as follows. Cyan (\square): semimetal, yellow (\square): topological band insulator and pink (\square): band insulator.

2. Split graph of line graph lattices $\mathcal{S}(\mathcal{L}(\mathcal{X}))$

The subdivision of the $2d - 2$ -regular line graphs $L(\mathcal{X}_i)$, where $i \in \{4, 6\}$, yields bipartite $(2d - 2, 2)$ -biregular graphs $\mathcal{S}(L(\mathcal{X}_i))$. These structures introduce additional blue sites positioned at the midpoint of the edges of the line graphs, as shown in Figs. 21a and 24a. By

definition, the blue atoms in both lattices are not directly connected to each other. In this study, we have also taken into account the interactions between these blue sites to explore their influence on the electronic and topological properties.

The schematic of the split of checkerboard lattice $S(L(\mathcal{X}_4))$ is shown in Fig. 21a. This structure can be interpreted as checkerboard lattice decorated with 90°-rotated square, each hosting an atom at the center. While the electronic and topological properties of many previously discussed structures have been studied, the $S(L(\mathcal{X}_4))$ graph remain unexplored.

The spinful Hamiltonian for the split graph of checkerboard lattice, $S(L(\mathcal{X}_4))$ can be written as

$$H_{S(L(\mathcal{X}_4))}(\mathbf{k}) = H_{S(L(\mathcal{X}_4))}^O(\mathbf{k}) \otimes \sigma_0 + H_{S(L(\mathcal{X}_4))}^{SO}(\mathbf{k}) \otimes \sigma_z, \quad (20)$$

where,

$$H_{S(L(\mathcal{X}_4))}^O(\mathbf{k}) = \begin{pmatrix} \mathcal{O}_{2 \times 2} & \Phi^\dagger(\mathbf{k}) \\ \Phi(\mathbf{k}) & \mathcal{M}_{5 \times 5}(\mathbf{k}) \end{pmatrix}, \quad H_{S(L(\mathcal{X}_4))}^{SO}(\mathbf{k}) = \begin{pmatrix} \mathcal{O}_{2 \times 2} & \mathcal{O}_{2 \times 5} \\ \mathcal{O}_{5 \times 2} & \mathcal{S}_{5 \times 5}(\mathbf{k}) \end{pmatrix} \quad (21)$$

where,

$$\Phi(\mathbf{k}) = \begin{pmatrix} t_1 & t_1 \\ t_1 e^{i\mathbf{k} \cdot \mathbf{a}_2} & t_1 \\ t_1 e^{i\mathbf{k} \cdot (\mathbf{a}_1 + \mathbf{a}_2)} & t_1 \\ t_1 e^{i\mathbf{k} \cdot \mathbf{a}_1} & t_1 \\ t_2(1 + e^{i\mathbf{k} \cdot \mathbf{a}_1}) & t_2(1 + e^{-i\mathbf{k} \cdot \mathbf{a}_2}) \end{pmatrix},$$

$$\mathcal{M}_{5 \times 5}(\mathbf{k}) = t_3 \begin{pmatrix} 0 & e^{i\mathbf{k} \cdot \mathbf{a}_2} & 0 & 1 & 1 \\ e^{-i\mathbf{k} \cdot \mathbf{a}_2} & 0 & 1 & 0 & e^{-i\mathbf{k} \cdot \mathbf{a}_2} \\ 0 & 1 & 0 & e^{-i\mathbf{k} \cdot \mathbf{a}_2} & e^{-i\mathbf{k} \cdot \mathbf{a}_2} \\ 1 & 0 & e^{i\mathbf{k} \cdot \mathbf{a}_2} & 0 & 1 \\ 1 & e^{i\mathbf{k} \cdot \mathbf{a}_2} & e^{i\mathbf{k} \cdot \mathbf{a}_2} & 1 & 0 \end{pmatrix} \quad \text{and}$$

$$\mathcal{S}_{5 \times 5}(\mathbf{k}) = i\lambda_I \begin{pmatrix} 0 & -1 & 0 & e^{i\mathbf{k} \cdot \mathbf{a}_1} & 0 \\ 1 & 0 & -e^{i\mathbf{k} \cdot \mathbf{a}_1} & 0 & 0 \\ 0 & e^{-i\mathbf{k} \cdot \mathbf{a}_1} & 0 & -1 & 0 \\ -e^{-i\mathbf{k} \cdot \mathbf{a}_1} & 0 & 1 & 0 & 0 \\ 0 & 0 & 0 & 0 & 0 \end{pmatrix}. \quad (22)$$

Here, the hopping parameters t_1 and t_2 describe the interactions between red atom and its neighboring blue atoms located at the edges and at the point of the intersections of diagonals, respectively. The third hopping parameter t_3 is connecting the blue atoms, which is 0 in the ideal $S(L(\mathcal{X}_4))$. While the checkerboard lattice has two sites in the unit cell, the $S(L(\mathcal{X}_4))$ has seven sites, resulting in seven electronic bands. The typical band structure with $t_3 = 0$ is shown in Fig. 21b. We find that the band diagram is mirror symmetric about the zero energy level. Remarkably, there are three overlapping flat bands which are degenerate with Dirac cones at the Γ -point similar to $\mathcal{S}(\mathcal{X}_4)$ graph (Lieb lattice). The Dirac bands are also degenerate with the parabolic band at M -point. Upon tuning t_3 , the three overlapping dispersionless bands split apart into partially dispersive bands with onset of tilted Dirac cones as shown in Fig. 22a. Finally, when all the hopping parameters are equal, the lowest energy band is isolated (see Fig. 22b).

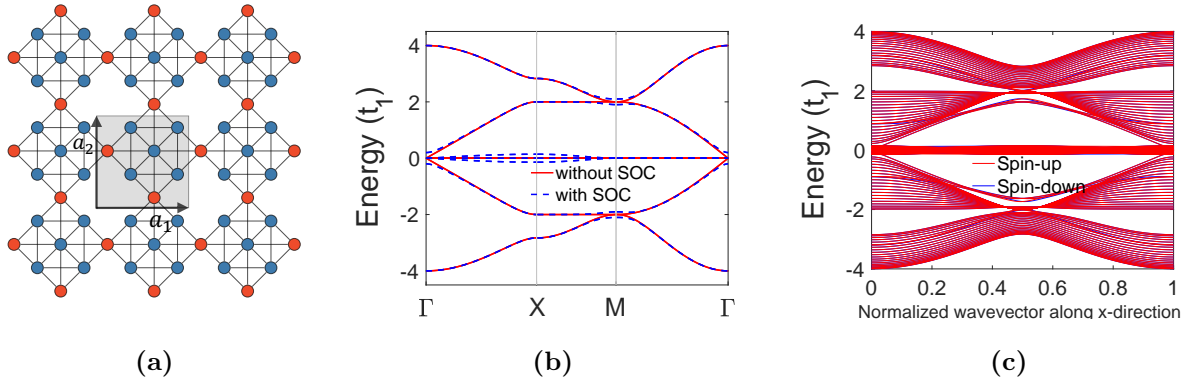


FIG. 21: (a) The split graph of the checkerboard lattice gives $S(L(\mathcal{X}_4))$. The black arrows indicate the lattice vectors \mathbf{a}_1 and \mathbf{a}_2 , and the gray region is the unit cell. The tight binding band diagram ($t_3 = 0$) of (b) 2D lattice without (red solid line) and with (blue broken line) SOC ($\lambda_I = 0.1t_1$) and (c) 1D zigzag lattice nanoribbon with $\lambda_I = 0.1t_1$. The red and blue lines show the counter-propagating spin-up and spin-down states, respectively.

Usually, inclusion of SOC isolated the bands and transforms the flatbands into quasiflat. Intriguingly, we observed that at $t_3 = 0$, the two out of three dispersionless bands at zero energy turn into non-degenerate quasiflat bands along the $\Gamma - X - M$ path (see dashed blue lines in Fig. 21b). However, the central flatband shows no dispersion in the entire BZ.

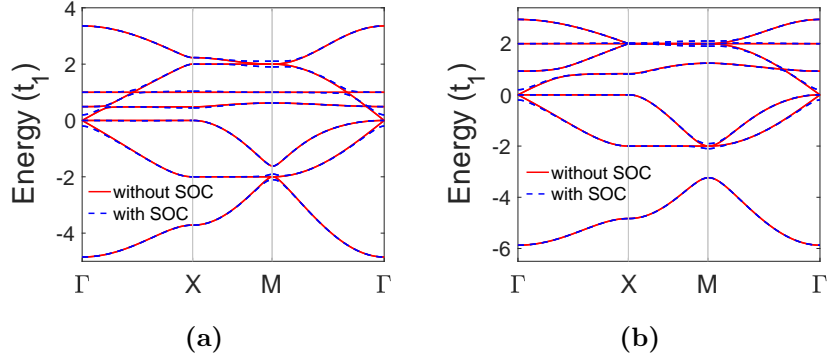


FIG. 22: The tight binding band diagram of checkerboard split graph $S(L(\mathcal{X}_4))$ at different values of t_3 . (a) $t_3 = 0.5t_1$ (b) $t_3 = t_1$. The solid red color lines is when $\lambda_I = 0$ and dashed blue lines when $\lambda_I = 0.1t_1$.

Fig. 23 shows the topological phases at $1/7$ filling fraction in $\epsilon_{xx} - \lambda_I$ space for different values of t_3 . The phase boundaries vary linearly with ϵ_{xx} . At $t_3 = 0.2t_1$, the topological non-trivial region sandwiched between the trivial insulator dominates the phase space as shown in Fig. 23a. With increasing t_3 , the non-trivial area shifts towards right and almost cover the entire phase diagram, as represented in Fig. 23c.

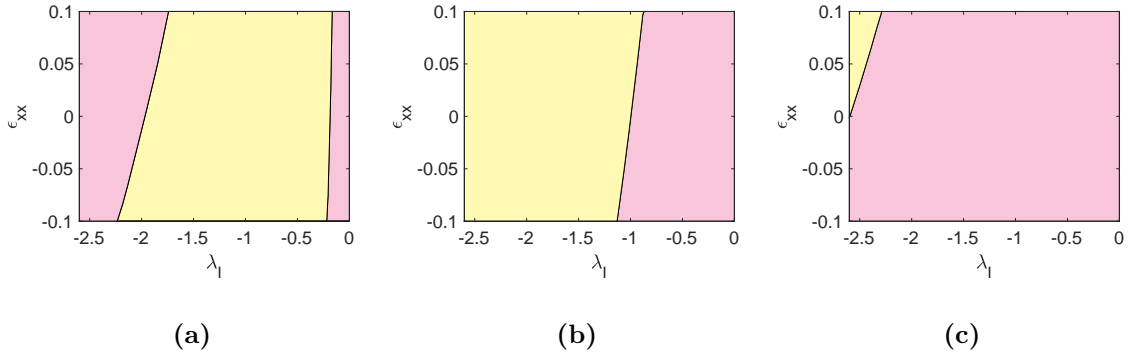


FIG. 23: Splitgraph of checkerboard lattice, $S(L(\mathcal{X}_4))$, at $1/7$ filling as the function of strain (ϵ_{xx}) and intrinsic spin orbit coupling (λ_I) at (a) $t_3 = 0.2t_1$ (b) $t_3 = 0.4t_1$, and (c) $t_3 = 0.6t_1$. The different phases are distinguished by the colors as follows. Yellow (\square): topological band insulator and pink (\square): band insulator.

The split graph of Kagome lattice $\mathcal{S}(L(\mathcal{X}_6))$ composed of two sublattices, as depicted in Fig. 24a. It contains nine atoms in the unit cell and can be viewed as triangles in triangles where red atoms sits at the Kagome sites and blue atoms form smaller equilateral triangles. According the the definition, of split graphs the blue atoms are not connected to each other. The magnetic properties of the lattice has been widely studied [138–142] but electronic and topological properties have not been well explored [143, 144].

The TB Hamiltonian of triangular Kagome lattice (TKL), $S(L(\mathcal{X}_6))$:

$$H_{S(L(\mathcal{X}_6))}(\mathbf{k}) = \begin{pmatrix} \mathcal{O}_{3 \times 3} & \mathcal{A}(\mathbf{k}) & \mathcal{B}(\mathbf{k}) \\ \mathcal{A}^\dagger(\mathbf{k}) & \mathcal{C}(\mathbf{k}) & \mathcal{O}_{3 \times 3} \\ \mathcal{B}^\dagger(\mathbf{k}) & \mathcal{O}_{3 \times 3} & \mathcal{D}(\mathbf{k}) \end{pmatrix} \otimes \sigma_0 + \begin{pmatrix} \mathcal{O}_{3 \times 3} & \mathcal{O}_{3 \times 3} & \mathcal{O}_{3 \times 3} \\ \mathcal{O}_{3 \times 3} & \mathcal{E}(\mathbf{k}) & \mathcal{O}_{3 \times 3} \\ \mathcal{O}_{3 \times 3} & \mathcal{O}_{3 \times 3} & \mathcal{F}(\mathbf{k}) \end{pmatrix} \otimes \sigma_z, \quad (23)$$

where,

$$\begin{aligned} \mathcal{A}(\mathbf{k}) &= t_{rb}(\Lambda_1 + \Lambda_3 + S_{11} + S_{33}), \\ \mathcal{B}(\mathbf{k}) &= t_{rb}(e^{i\mathbf{k} \cdot \mathbf{a}_1}(S_{11} + S_{33}), + e^{i\mathbf{k} \cdot \mathbf{a}_2}(S_{12} + S_{23}) + S_{21} + S_{32}) \\ \mathcal{C}(\mathbf{k}) &= t_{bb} \sum_{i=1}^3 \Lambda_i, \\ \mathcal{D}(\mathbf{k}) &= t_{bb} \left(\sum_{i=1}^3 (\cos \mathbf{k} \cdot \mathbf{a}_{4-i}) \Lambda_i - \sin \mathbf{k} \cdot \mathbf{a}_3 \Lambda_4 + \sin \mathbf{k} \cdot \mathbf{a}_2 \Lambda_5 + \sin \mathbf{k} \cdot \mathbf{a}_1 \Lambda_6 \right), \\ \mathcal{E}(\mathbf{k}) &= \lambda_I \sum_{i=4}^6 (-1)^{i-1} \Lambda_i, \quad \text{and} \\ \mathcal{F}(\mathbf{k}) &= \lambda_I \left(-\cos \mathbf{k} \cdot \mathbf{a}_3 \Lambda_4 + \cos \mathbf{k} \cdot \mathbf{a}_2 \Lambda_5 - \cos \mathbf{k} \cdot \mathbf{a}_1 \Lambda_6 + \sum_{i=1}^3 (-1)^i \sin \mathbf{k} \cdot \mathbf{a}_{4-i} \Lambda_i \right). \end{aligned} \quad (24)$$

where, t_{rb} and t_{bb} are the hopping energies between red-blue and blue-blue atoms, respectively. Compared to Kagome lattice, TKL structure exhibit enhanced frustration which makes it advantageous in hosting various dispersionless bands and topological states. When $t_{bb} = 0$ and $\lambda_I = 0$, the spectrum of $\mathcal{S}(L(\mathcal{X}_6))$ contains three degenerate isolated flat bands at $E = 0$ and two groups of Kagome-type bands that are mirror symmetric around $E = 0$, as depicted in Fig. 24b. These gapped perfect flatbands that do not interact any dispersive bands are known to enhance the Coulomb interaction, thus leading to strongly correlated behavior [31, 145]. For example, superconductivity in moiré superlattices in magic angle

twisted bilayer graphene [11, 12]. In most of the systems, to obtain such electronic properties often require some degree of engineering and fine control of system parameters such as twist angle, magnetic field strength, symmetry breaking potentials and SOC [121, 146, 147]. Therefore, if TKL is realized in a natural atomic arrangement of the material, it could be fascinating. Moreover, we found that the $E = 0$ flat bands are resilient against deformation hence preserves strongly correlated states.

The structure with blue colored atoms connected can be constructed by series of graph operation, specifically $L(L(\mathcal{S}(\mathcal{X}_6)))$. Tuning t_{bb} , introduces three sets of Kagome-like bands at $t_{bb} = 0.2t_{rb}$ (see Fig. 25a) which are known to exhibit tilted Dirac cones under lattice deformation. During the tuning process, there is point when $t_{bb} = \frac{1}{\sqrt{3}}t_{rb}$, the three bands touches at the Γ -point and form HK lattice-like ($\mathcal{S}(\mathcal{X}_6)$) pseudospin-1 states, in Fig. 24b. At $t_{bb} = 1$ limit, the three isolated overlapping flat bands appear again but at the top of the band structure (Fig. 24c).

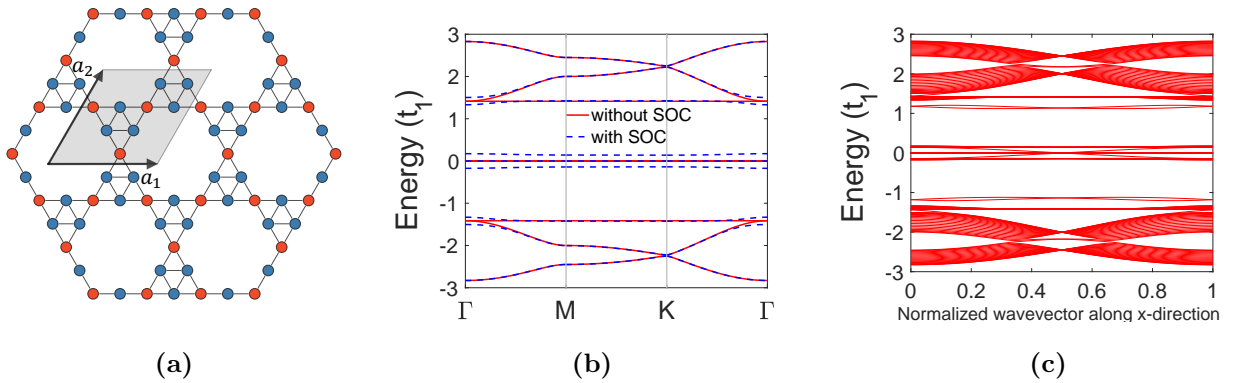


FIG. 24: (a) Triangular kagome lattice obtained by applying the split graph operation on the kagome lattice, $S(L(\mathcal{X}_6))$. The black arrows indicate the lattice vectors \mathbf{a}_1 and \mathbf{a}_2 , and the gray region is the unit cell. The tight binding band diagram ($t_{bb} = 0$) of (b) 2D lattice without (red solid line) and with (blue broken line) SOC ($\lambda_I = 0.1t$) and (c) 1D zigzag lattice nanoribbon with $\lambda_I = 0.1t$. The red and blue lines show the counter-propagating spin-up and spin-down states, respectively.

Exhibiting large number of bands than kagome lattice, TKL phase diagrams shows all kind of phases discussed above. Figures 26 to 29 show the strain-SOC phase diagrams

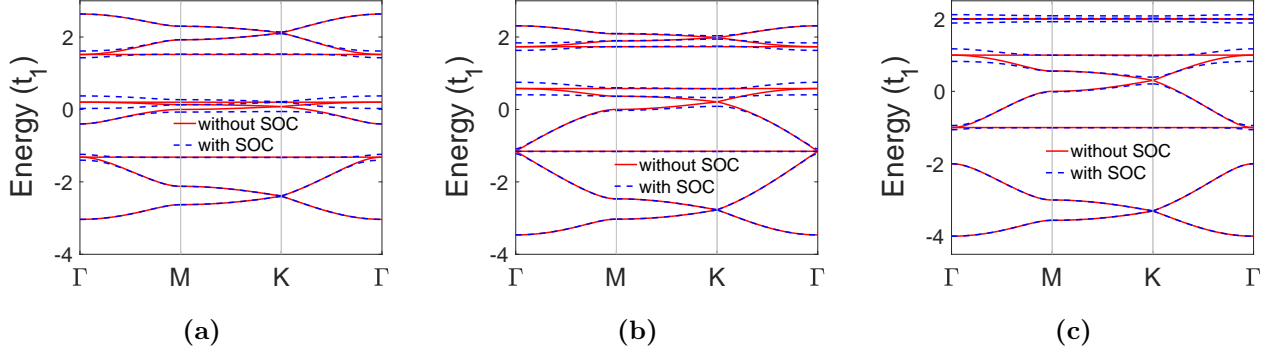


FIG. 25: The tight binding band structure of triangular Kagome lattice $L(L(\mathcal{S}(\mathcal{X}_6)))$ at different values of t_{bb} . (a) $t_{bb} = 0.2t_{rb}$, (b) $t_{bb} = \frac{1}{\sqrt{3}}t_{rb}$ and (c) $t_{bb} = t_{rb}$. The solid red color lines is when $\lambda_I = 0$ and dashed blue lines when $\lambda_I = 0.1t_1$.

at different filling fractions for different values of t_{bb} . Mostly, the phase boundaries shows linear relationship with the phase variables. By definition, two topological distinct phases are separated by the band crossing point. Remarkably, in some cases, we noticed that in some cases $2/9$ (Fig. 26), $5/9$ (Fig. 28) and $7/9$ (Fig. 29) filling fractions there is line of TKL showing DSM phase (shown by red line) lying in the topological region in some cases. At this line, the band gap vanishes but the system does not undergo topological phase transition. There is an onset of ordinary semimetal phase at the fourth and fifth band at different values of t_{bb} , as depicted in Figs. 27 and 28, respectively.

IV. CONCLUSION

In summary, we have demonstrated the rich landscape of topological phase transitions in 2D flat-band lattices, as induced by strain. By leveraging graph-theoretic transformations on root bipartite lattices, we systematically explored how split and line graph operations can yield unique (and sometimes unexplored) 2D lattices with tunable electronic and topological properties. Our findings reveal that strategically applied strain induces various phase transitions in these lattices, including those between trivial and topological insulators, as well as semimetallic and Dirac phases. Moreover, our results underscore how strain not only

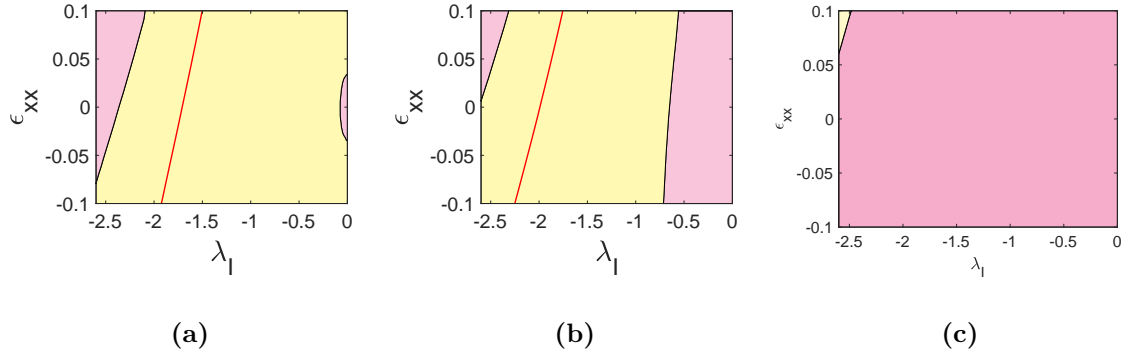


FIG. 26: Topological phase diagram of triangular kagome lattice, $S(L(\mathcal{X}_6))$, at $2/9$ filling as the function of strain (ϵ_{xx}) and intrinsic spin orbit coupling (λ_I) at (a) $t_{bb} = 0.6t_{rb}$, (b) $t_{bb} = 0.8t_{rb}$, and (c) $t_{bb} = 1.8t_{rb}$. The different phases are distinguished by the colors as follows. Cyan (\square): semimetal, yellow (\square): topological band insulator, and pink (\square): band insulator.

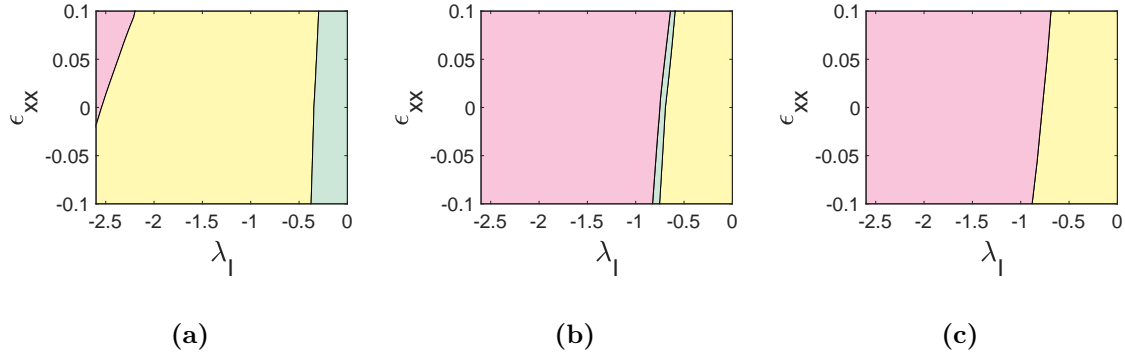


FIG. 27: Topological phase diagram of triangular kagome lattice, $S(L(\mathcal{X}_6))$, at $4/9$ filling as the function of strain (ϵ_{xx}) and intrinsic spin orbit coupling (λ_I) at (a) $t_{bb} = 0.2t_{rb}$ (b) $t_{bb} = 0.4t_{rb}$, and (c) $t_{bb} = 0.6t_{rb}$. The different phases are distinguished by the colors as follows. Yellow (\square): topological band insulator and pink (\square): band insulator.

distorts lattice symmetries but also introduces new Dirac points, tilting and merging them to yield complex phase landscapes, including transitions from quadratic band crossing to tilted Dirac cones. These behaviors highlights the critical role of structural deformations in modulating electronic band structures in these systems, showcasing strain as a viable method for engineering the quantum phases of 2D materials with minimal external interference. Indeed,

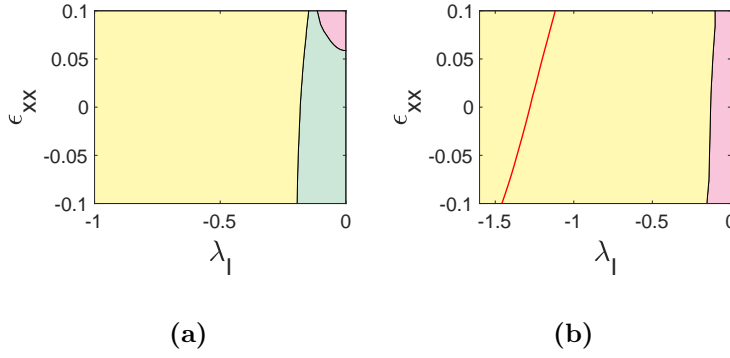


FIG. 28: Topological phase diagram of triangular kagome lattice, $S(L(\mathcal{X}_6))$, at 5/9 filling as the function of strain (ϵ_{xx}) and intrinsic spin orbit coupling (λ_I) at (a) $t_{bb} = 0.4t_{rb}$ and (b) $t_{bb} = 1.8t_{rb}$. The different phases are distinguished by the colors as follows. Cyan (\square): semimetal, yellow (\square): topological band insulator and pink (\square): band insulator.

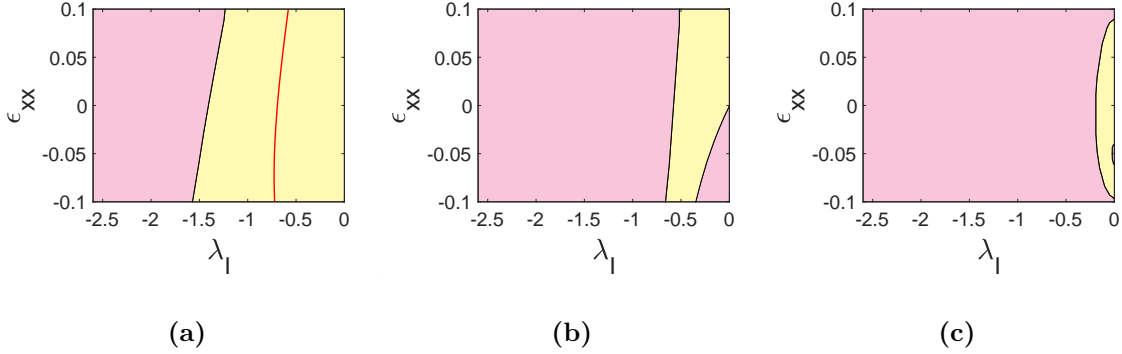


FIG. 29: Topological phase diagram of triangular kagome lattice, $S(L(\mathcal{X}_6))$, at 7/9 filling as the function of strain (ϵ_{xx}) and intrinsic spin orbit coupling (λ_I) at (a) $t_{bb} = 0.2t_{rb}$, (b) $t_{bb} = 1t_{rb}$ and (c) $t_{bb} = 2.6t_{rb}$. The different phases are distinguished by the colors as follows. Yellow (\square): topological band insulator and pink (\square): band insulator.

it is easily conceivable that in experimental settings such strains can be applied through substrates or device contacts, thus bringing forth or suppressing such transitions in a controllable manner. Our study further illustrates the utility of graph-theoretic frameworks in constructing and understanding higher-generation lattices from existing ones, thus providing deterministic recipes of generating structures with desirable electronic properties.

The topological robustness observed in these systems under certain conditions, specifically with the inclusion of spin-orbit coupling (SOC), opens potential pathways for applications in quantum spintronics and topologically protected transport. Importantly, the ability to achieve type-I and type-II Dirac fermions through strain in specific lattice configurations suggests new avenues for realizing exotic quasiparticles with tailored dispersion properties. Overall, our work aims to provide a foundational understanding that could inform experimental pursuits aimed at synthesizing 2D materials with tunable topological characteristics, thus marking a significant step toward the practical application of topological materials in future quantum and microelectronics technologies.

—

Appendix A: Gell-Mann matrices

The Gell-Mann matrices are:

$$\Lambda_1 = \begin{pmatrix} 0 & 1 & 0 \\ 1 & 0 & 0 \\ 0 & 0 & 0 \end{pmatrix}, \quad \Lambda_2 = \begin{pmatrix} 0 & 0 & 1 \\ 0 & 0 & 0 \\ 1 & 0 & 0 \end{pmatrix}, \quad \Lambda_3 = \begin{pmatrix} 0 & 0 & 0 \\ 0 & 0 & 1 \\ 0 & 1 & 0 \end{pmatrix}, \quad \Lambda_4 = \begin{pmatrix} 0 & -i & 0 \\ i & 0 & 0 \\ 0 & 0 & 0 \end{pmatrix},$$

$$\Lambda_5 = \begin{pmatrix} 0 & 0 & -i \\ 0 & 0 & 0 \\ i & 0 & 0 \end{pmatrix}, \quad \Lambda_6 = \begin{pmatrix} 0 & 0 & 0 \\ 0 & 0 & -i \\ 0 & i & 0 \end{pmatrix}, \quad \Lambda_7 = \begin{pmatrix} 1 & 0 & 0 \\ 0 & -1 & 0 \\ 0 & 0 & 0 \end{pmatrix}, \quad \Lambda_8 = \frac{1}{\sqrt{3}} \begin{pmatrix} 1 & 0 & 0 \\ 0 & 1 & 0 \\ 0 & 0 & -2 \end{pmatrix}. \quad (\text{A1})$$

ACKNOWLEDGEMENTS

This work was primarily supported by grant DE-SC0023432 funded by the U.S. Department of Energy, Office of Science. Additionally, the work of SS at the University of Minnesota was supported by DoD Grant No. N00014-19-1-2623. This research used resources of the National Energy Research Scientific Computing Center, a DOE Office of Science User Facility supported by the Office of Science of the U.S. Department of Energy under Contract No. DE-AC02-05CH11231, using NERSC awards BES-ERCAP0025205, BES-ERCAP0025168, and

BES-ERCAP0028072. ASB acknowledges startup support from the Samueli School Of Engineering at UCLA, as well as support through a Faculty Career Development Award from UCLA's Office of Equity, Diversity and Inclusion. SS would like thank Richard D. James (University of Minnesota, Minneapolis) for insightful discussions and for providing support through the Vannevar Bush Faculty Fellowship. The authors acknowledge the use of the GPT-4 (OpenAI) model to polish the language and edit grammatical errors in some sections of this manuscript. The authors subsequently inspected, validated and edited the text generated by the AI model, before incorporation.

- [1] Y. Tokura, M. Kawasaki, and N. Nagaosa, *Nature Physics* **13**, 1056 (2017).
- [2] N. P. De Leon, K. M. Itoh, D. Kim, K. K. Mehta, T. E. Northup, H. Paik, B. Palmer, N. Samarth, S. Sangtawesin, and D. W. Steuerman, *Science* **372**, eabb2823 (2021).
- [3] F. Giustino, J. H. Lee, F. Trier, M. Bibes, S. M. Winter, R. Valentí, Y.-W. Son, L. Taillefer, C. Heil, A. I. Figueroa, *et al.*, *Journal of Physics: Materials* **3**, 042006 (2021).
- [4] D. Basov, R. Averitt, and D. Hsieh, *Nature materials* **16**, 1077 (2017).
- [5] R. Mas-Balleste, C. Gomez-Navarro, J. Gomez-Herrero, and F. Zamora, *Nanoscale* **3**, 20 (2011).
- [6] C. D. Aiello, J. M. Abendroth, M. Abbas, A. Afanasev, S. Agarwal, A. S. Banerjee, D. N. Beratan, J. N. Belling, B. Berche, A. Botana, *et al.*, *ACS nano* **16**, 4989 (2022).
- [7] A. H. Castro Neto, F. Guinea, N. M. Peres, K. S. Novoselov, and A. K. Geim, *Reviews of modern physics* **81**, 109 (2009).
- [8] L. A. Falkovsky, in *Journal of Physics: conference series* (IOP Publishing, 2008) p. 012004.
- [9] N. M. Peres, *Reviews of modern physics* **82**, 2673 (2010).
- [10] K. K. Gomes, W. Mar, W. Ko, F. Guinea, and H. C. Manoharan, *Nature* **483**, 306 (2012).
- [11] Y. Cao, V. Fatemi, S. Fang, K. Watanabe, T. Taniguchi, E. Kaxiras, and P. Jarillo-Herrero, *Nature* **556**, 43 (2018).
- [12] Y. Cao, V. Fatemi, A. Demir, S. Fang, S. L. Tomarken, J. Y. Luo, J. D. Sanchez-Yamagishi, K. Watanabe, T. Taniguchi, E. Kaxiras, *et al.*, *Nature* **556**, 80 (2018).

- [13] A. Mielke, *Physics Letters A* **174**, 443 (1993).
- [14] I. Hase, T. Yanagisawa, Y. Aiura, and K. Kawashima, *Physical review letters* **120**, 196401 (2018).
- [15] A. L. Sharpe, E. J. Fox, A. W. Barnard, J. Finney, K. Watanabe, T. Taniguchi, M. Kastner, and D. Goldhaber-Gordon, *Science* **365**, 605 (2019).
- [16] Y. Saito, J. Ge, L. Rademaker, K. Watanabe, T. Taniguchi, D. A. Abanin, and A. F. Young, *Nature Physics* **17**, 478 (2021).
- [17] H. Aoki, *Journal of Superconductivity and Novel Magnetism* **33**, 2341 (2020).
- [18] L. Balents, C. R. Dean, D. K. Efetov, and A. F. Young, *Nature Physics* **16**, 725 (2020).
- [19] X. Liu, C.-L. Chiu, J. Y. Lee, G. Farahi, K. Watanabe, T. Taniguchi, A. Vishwanath, and A. Yazdani, *Nature communications* **12**, 2732 (2021).
- [20] V. Peri, Z.-D. Song, B. A. Bernevig, and S. D. Huber, *Physical review letters* **126**, 027002 (2021).
- [21] C. Wu, D. Bergman, L. Balents, and S. Das Sarma, *Physical review letters* **99**, 070401 (2007).
- [22] Y. Chen, S. Xu, Y. Xie, C. Zhong, C. Wu, and S. Zhang, *Physical Review B* **98**, 035135 (2018).
- [23] F. Wang and Y. Ran, *Physical Review B—Condensed Matter and Materials Physics* **84**, 241103 (2011).
- [24] N. Regnault and B. A. Bernevig, *Physical Review X* **1**, 021014 (2011).
- [25] Z. Liu, E. J. Bergholtz, H. Fan, and A. M. Läuchli, *Physical review letters* **109**, 186805 (2012).
- [26] E. J. Bergholtz and Z. Liu, *International Journal of Modern Physics B* **27**, 1330017 (2013).
- [27] K. Sun, Z. Gu, H. Katsura, and S. Das Sarma, *Physical review letters* **106**, 236803 (2011).
- [28] E. Tang, J.-W. Mei, and X.-G. Wen, *Physical review letters* **106**, 236802 (2011).
- [29] T. Neupert, L. Santos, C. Chamon, and C. Mudry, *Physical review letters* **106**, 236804 (2011).
- [30] T. Neupert, L. Santos, S. Ryu, C. Chamon, and C. Mudry, *Physical review letters* **108**, 046806 (2012).

- [31] G. Tarnopolsky, A. J. Kruchkov, and A. Vishwanath, *Physical review letters* **122**, 106405 (2019).
- [32] H. C. Po, L. Zou, A. Vishwanath, and T. Senthil, *Physical Review X* **8**, 031089 (2018).
- [33] H. Isobe, N. F. Yuan, and L. Fu, *Physical Review X* **8**, 041041 (2018).
- [34] M. Kang, S. Fang, L. Ye, H. C. Po, J. Denlinger, C. Jozwiak, A. Bostwick, E. Rotenberg, E. Kaxiras, J. G. Checkelsky, *et al.*, *Nature communications* **11**, 4004 (2020).
- [35] Z. Liu, M. Li, Q. Wang, G. Wang, C. Wen, K. Jiang, X. Lu, S. Yan, Y. Huang, D. Shen, *et al.*, *Nature communications* **11**, 4002 (2020).
- [36] J.-X. Yin, S. S. Zhang, G. Chang, Q. Wang, S. S. Tsirkin, Z. Guguchia, B. Lian, H. Zhou, K. Jiang, I. Belopolski, *et al.*, *Nature Physics* **15**, 443 (2019).
- [37] M. Kang, L. Ye, S. Fang, J.-S. You, A. Levitan, M. Han, J. I. Facio, C. Jozwiak, A. Bostwick, E. Rotenberg, *et al.*, *Nature materials* **19**, 163 (2020).
- [38] Z. Lin, J.-H. Choi, Q. Zhang, W. Qin, S. Yi, P. Wang, L. Li, Y. Wang, H. Zhang, Z. Sun, *et al.*, *Physical review letters* **121**, 096401 (2018).
- [39] D. Di Sante, C. Bigi, P. Eck, S. Enzner, A. Consiglio, G. Pokharel, P. Carrara, P. Orgiani, V. Polewczyk, J. Fujii, *et al.*, *Nature Physics* **19**, 1135 (2023).
- [40] Z. Zhang, Y. Wang, K. Watanabe, T. Taniguchi, K. Ueno, E. Tutuc, and B. J. LeRoy, *Nature Physics* **16**, 1093 (2020).
- [41] D. Leykam, A. Andreanov, and S. Flach, *Advances in Physics: X* **3**, 1473052 (2018).
- [42] S. Mukherjee, M. Di Liberto, P. Öhberg, R. R. Thomson, and N. Goldman, *Physical review letters* **121**, 075502 (2018).
- [43] J. Ma, J.-W. Rhim, L. Tang, S. Xia, H. Wang, X. Zheng, S. Xia, D. Song, Y. Hu, Y. Li, B.-J. Yang, D. Leykam, and Z. Chen, [Phys. Rev. Lett.](#) **124**, 183901 (2020).
- [44] D. Guzmán-Silva, C. Mejía-Cortés, M. Bandres, M. Rechtsman, S. Weimann, S. Nolte, M. Segev, A. Szameit, and R. Vicencio, *New Journal of Physics* **16**, 063061 (2014).
- [45] R. A. Vicencio, C. Cantillano, L. Morales-Inostroza, B. Real, C. Mejía-Cortés, S. Weimann, A. Szameit, and M. I. Molina, *Physical review letters* **114**, 245503 (2015).
- [46] S. Mukherjee, A. Spracklen, D. Choudhury, N. Goldman, P. Öhberg, E. Andersson, and R. R. Thomson, *Physical review letters* **114**, 245504 (2015).

- [47] J. Ma, J.-W. Rhim, L. Tang, S. Xia, H. Wang, X. Zheng, S. Xia, D. Song, Y. Hu, Y. Li, *et al.*, *Physical Review Letters* **124**, 183901 (2020).
- [48] M. Milićević, G. Montambaux, T. Ozawa, O. Jamadi, B. Real, I. Sagnes, A. Lemaître, L. Le Gratiet, A. Harouri, J. Bloch, *et al.*, *Physical Review X* **9**, 031010 (2019).
- [49] A. J. Kollár, M. Fitzpatrick, and A. A. Houck, *Nature* **571**, 45 (2019).
- [50] G.-B. Jo, J. Guzman, C. K. Thomas, P. Hosur, A. Vishwanath, and D. M. Stamper-Kurn, *Phys. Rev. Lett.* **108**, 045305 (2012).
- [51] Y. He, R. Mao, H. Cai, J.-X. Zhang, Y. Li, L. Yuan, S.-Y. Zhu, and D.-W. Wang, *Phys. Rev. Lett.* **126**, 103601 (2021).
- [52] X. Zhou, Y. Chen, J. Chen, C. Hu, B. Lyu, K. Xu, S. Lou, P. Shen, S. Ma, Z. Wu, *et al.*, *Physical Review B* **109**, 045105 (2024).
- [53] O. Arroyo-Gascón, R. Fernández-Perea, E. S. Morell, C. Cabrillo, and L. Chico, *Carbon* **205**, 394 (2023).
- [54] O. Arroyo-Gascón, R. Fernández-Perea, E. Suarez Morell, C. Cabrillo, and L. Chico, *Nano Letters* **20**, 7588 (2020).
- [55] H. M. Yu, S. Sharma, S. Agarwal, O. Liebman, and A. S. Banerjee, *RSC advances* **14**, 963 (2024).
- [56] S. Sharma, C. Wang, H. M. Yu, and A. S. Banerjee, arXiv preprint arXiv:submit/6142213 (2025).
- [57] A. S. Banerjee and P. Suryanarayana, *Journal of the Mechanics and Physics of Solids* **96**, 605 (2016).
- [58] A. S. Banerjee, *Journal of the Mechanics and Physics of Solids* **154**, 104515 (2021).
- [59] S. Ghosh, A. S. Banerjee, and P. Suryanarayana, *Physical Review B* **100**, 125143 (2019).
- [60] H. M. Yu and A. S. Banerjee, *Journal of Computational Physics* **456**, 111023 (2022).
- [61] S. Pathrudkar, H. M. Yu, S. Ghosh, and A. S. Banerjee, *Physical Review B* **105**, 195141 (2022).
- [62] S. Agarwal and A. S. Banerjee, *Journal of Computational Physics* **496**, 112551 (2024).
- [63] D. Basov and A. V. Chubukov, *Nature Physics* **7**, 272 (2011).
- [64] S. Peotta and P. Törmä, *Nature communications* **6**, 8944 (2015).

- [65] F. Xie, Z. Song, B. Lian, and B. A. Bernevig, Physical review letters **124**, 167002 (2020).
- [66] Z. Song, Z. Wang, W. Shi, G. Li, C. Fang, and B. A. Bernevig, Physical review letters **123**, 036401 (2019).
- [67] H. C. Po, L. Zou, T. Senthil, and A. Vishwanath, Physical Review B **99**, 195455 (2019).
- [68] J. Ahn, S. Park, and B.-J. Yang, Physical Review X **9**, 021013 (2019).
- [69] A. Julku, T. J. Peltonen, L. Liang, T. T. Heikkilä, and P. Törmä, Physical Review B **101**, 060505 (2020).
- [70] H. Tian, S. Che, T. Xu, P. Cheung, K. Watanabe, T. Taniguchi, M. Randeria, F. Zhang, C. N. Lau, and M. W. Bockrath, arXiv preprint arXiv:2112.13401 (2021).
- [71] N. Kopnin, T. Heikkilä, and G. Volovik, Physical Review B—Condensed Matter and Materials Physics **83**, 220503 (2011).
- [72] A. Lau, T. Hyart, C. Autieri, A. Chen, and D. I. Pikulin, Physical Review X **11**, 031017 (2021).
- [73] K. v. Klitzing, G. Dorda, and M. Pepper, Physical review letters **45**, 494 (1980).
- [74] A. J. Heeger, S. Kivelson, J. R. Schrieffer, and W.-P. Su, Reviews of Modern Physics **60**, 781 (1988).
- [75] S. Kivelson and D. Heim, Physical Review B **26**, 4278 (1982).
- [76] C. L. Kane and E. J. Mele, Physical review letters **95**, 226801 (2005).
- [77] C. L. Kane and E. J. Mele, Physical review letters **95**, 146802 (2005).
- [78] M. Z. Hasan and C. L. Kane, Reviews of modern physics **82**, 3045 (2010).
- [79] B. A. Bernevig, T. L. Hughes, and S.-C. Zhang, science **314**, 1757 (2006).
- [80] H. C. Po, H. Watanabe, and A. Vishwanath, Physical review letters **121**, 126402 (2018).
- [81] C. Xu and J. E. Moore, Physical Review B—Condensed Matter and Materials Physics **73**, 045322 (2006).
- [82] C. Wu, B. A. Bernevig, and S.-C. Zhang, Physical review letters **96**, 106401 (2006).
- [83] K. Sun, H. Yao, E. Fradkin, and S. A. Kivelson, Physical review letters **103**, 046811 (2009).
- [84] M. Mojarro and S. E. Ulloa, 2D Materials **11**, 011001 (2023).
- [85] A. Rüegg, J. Wen, and G. A. Fiete, Physical Review B—Condensed Matter and Materials Physics **81**, 205115 (2010).

- [86] H.-M. Guo and M. Franz, *Physical Review B—Condensed Matter and Materials Physics* **80**, 113102 (2009).
- [87] C. Weeks and M. Franz, *Physical Review B—Condensed Matter and Materials Physics* **82**, 085310 (2010).
- [88] S. Flach, D. Leykam, J. D. Bodyfelt, P. Matthies, and A. S. Desyatnikov, *Europhysics Letters* **105**, 30001 (2014).
- [89] Y. Xu and H. Pu, *Physical Review A* **102**, 053305 (2020).
- [90] A. J. Kollár, M. Fitzpatrick, P. Sarnak, and A. A. Houck, *Communications in Mathematical Physics* **376**, 1909 (2020).
- [91] D.-S. Ma, Y. Xu, C. S. Chiu, N. Regnault, A. A. Houck, Z. Song, and B. A. Bernevig, *Physical review letters* **125**, 266403 (2020).
- [92] S. Miyahara, K. Kubo, H. Ono, Y. Shimomura, and N. Furukawa, *Journal of the Physical Society of Japan* **74**, 1918 (2005).
- [93] A. Mielke, *Journal of Physics A: Mathematical and General* **24**, L73 (1991).
- [94] A. Mielke, *Journal of Physics A: Mathematical and General* **24**, 3311 (1991).
- [95] D. L. Bergman, C. Wu, and L. Balents, *Physical Review B—Condensed Matter and Materials Physics* **78**, 125104 (2008).
- [96] J. M. Kim, M. F. Haque, E. Y. Hsieh, S. M. Nahid, I. Zarin, K.-Y. Jeong, J.-P. So, H.-G. Park, and S. Nam, *Advanced Materials* **35**, 2107362 (2023).
- [97] Z. Dai, L. Liu, and Z. Zhang, *Advanced Materials* **31**, 1805417 (2019).
- [98] P. Borlido, A. W. Huran, M. A. Marques, and S. Botti, *npj 2D Materials and Applications* **3**, 21 (2019).
- [99] K. R. Abidi and P. Koskinen, *Nanoscale* **16**, 19649 (2024).
- [100] Y. Chen, Y. Lei, Y. Li, Y. Yu, J. Cai, M.-H. Chiu, R. Rao, Y. Gu, C. Wang, W. Choi, *et al.*, *Nature* **577**, 209 (2020).
- [101] J. P. Ruf, H. Paik, N. J. Schreiber, H. P. Nair, L. Miao, J. K. Kawasaki, J. N. Nelson, B. D. Faeth, Y. Lee, B. H. Goodge, *et al.*, *Nature Communications* **12**, 59 (2021).
- [102] M. Doob and H. Sachs, *Spectra of Graphs: Theory and Application* (Deutscher Verlag der Wissenschaften, 1980).

- [103] M. Desai and V. Rao, *Journal of Graph Theory* **18**, 181 (1994).
- [104] C. S. Chiu, D.-S. Ma, Z.-D. Song, B. A. Bernevig, and A. A. Houck, *Phys. Rev. Res.* **2**, 043414 (2020).
- [105] G. Sethi, B. Xia, D. Kim, H. Liu, X. Li, and F. Liu, *Physical Review B* **109**, 035140 (2024).
- [106] L.-K. Lim, J.-N. Fuchs, F. Piéchon, and G. Montambaux, *Physical Review B* **101**, 045131 (2020).
- [107] W. Jiang, M. Kang, H. Huang, H. Xu, T. Low, and F. Liu, *Physical Review B* **99**, 125131 (2019).
- [108] G. Montambaux, L.-K. Lim, J.-N. Fuchs, and F. Piéchon, *Physical review letters* **121**, 256402 (2018).
- [109] J.-W. Rhim and B.-J. Yang, *Physical Review B* **99**, 045107 (2019).
- [110] T. Mohiuddin, A. Lombardo, R. Nair, A. Bonetti, G. Savini, R. Jalil, N. Bonini, D. Basko, C. Galotis, N. Marzari, *et al.*, *Physical Review B—Condensed Matter and Materials Physics* **79**, 205433 (2009).
- [111] A. A. Soluyanov and D. Vanderbilt, *Physical Review B—Condensed Matter and Materials Physics* **83**, 235401 (2011).
- [112] D. Gresch, G. Autes, O. V. Yazyev, M. Troyer, D. Vanderbilt, B. A. Bernevig, and A. A. Soluyanov, *Physical Review B* **95**, 075146 (2017).
- [113] S. Ryu and Y. Hatsugai, *Phys. Rev. Lett.* **89**, 077002 (2002).
- [114] B. A. Bernevig, *Topological insulators and topological superconductors* (Princeton university press, 2013).
- [115] A. Burkov, *Nature materials* **15**, 1145 (2016).
- [116] J. Ahn and B.-J. Yang, *Physical Review Letters* **118**, 156401 (2017).
- [117] A. H. Nevidomskyy, C. Scheiber, D. Sénéchal, and A.-M. Tremblay, *Physical Review B—Condensed Matter and Materials Physics* **77**, 064427 (2008).
- [118] M. Z. Asadzadeh, M. Fabrizio, and F. Becca, *Physical Review B* **90**, 205113 (2014).
- [119] T. Kariyado and A. Vishwanath, *Physical Review Research* **1**, 033076 (2019).
- [120] V. M. Pereira, A. Castro Neto, and N. Peres, *Physical Review B—Condensed Matter and Materials Physics* **80**, 045401 (2009).

- [121] D. Green, L. Santos, and C. Chamon, *Physical Review B—Condensed Matter and Materials Physics* **82**, 075104 (2010).
- [122] D. Bercioux, D. Urban, H. Grabert, and W. Häusler, *Physical Review A—Atomic, Molecular, and Optical Physics* **80**, 063603 (2009).
- [123] T. Mizoguchi, Y. Kuno, and Y. Hatsugai, *Physical Review A* **102**, 033527 (2020).
- [124] T. Mizoguchi, T. Yoshida, and Y. Hatsugai, *Physical Review B* **103**, 045136 (2021).
- [125] W. Li, D. Sheng, C. Ting, and Y. Chen, *Physical Review B* **90**, 081102 (2014).
- [126] D. Sheng, Z.-C. Gu, K. Sun, and L. Sheng, *Nature communications* **2**, 389 (2011).
- [127] A. Bolens and N. Nagaosa, *Physical Review B* **99**, 165141 (2019).
- [128] A. Bao, H.-S. Tao, H.-D. Liu, X. Zhang, and W.-M. Liu, *Scientific reports* **4**, 6918 (2014).
- [129] M. Kargarian and G. A. Fiete, *Physical Review B—Condensed Matter and Materials Physics* **82**, 085106 (2010).
- [130] G.-X. Wang and Y.-Z. Zhang, *Physics Letters A* **419**, 127743 (2021).
- [131] Y. Yang, J. Yang, X. Li, and Y. Zhao, *Physics Letters A* **382**, 723 (2018).
- [132] Y.-T. Kang, C. Lu, F. Yang, and D.-X. Yao, *Physical Review B* **99**, 184506 (2019).
- [133] Y. Yamashita, M. Tomura, Y. Yanagi, and K. Ueda, *Physical Review B—Condensed Matter and Materials Physics* **88**, 195104 (2013).
- [134] D. Oriekhov, V. Gusynin, and V. Loktev, *Physical Review B* **103**, 195104 (2021).
- [135] A. Sil and A. K. Ghosh, *Journal of Physics: Condensed Matter* **31**, 245601 (2019).
- [136] Y. Chen, Y. Sun, H. Wang, D. West, Y. Xie, J. Zhong, V. Meunier, M. L. Cohen, and S. Zhang, *Physical review letters* **113**, 085501 (2014).
- [137] B. Sarikavak-Lisesivdin, S. Lisesivdin, E. Ozbay, and F. Jelezko, *Chemical physics letters* **760**, 138006 (2020).
- [138] M. Isoda, H. Nakano, and T. Sakai, *Journal of the Physical Society of Japan* **81**, 053703 (2012).
- [139] Y. L. Loh, D.-X. Yao, and E. W. Carlson, *Physical Review B—Condensed Matter and Materials Physics* **77**, 134402 (2008).
- [140] M.-H. Zhang and D.-X. Yao, *Physical Review B* **107**, 024408 (2023).
- [141] C. Zhou, Y. Feng, J. Ruan, and D.-X. Yao, *Physical Review E* **98**, 012127 (2018).

- [142] D.-X. Yao, Y. L. Loh, E. W. Carlson, and M. Ma, *Physical Review B—Condensed Matter and Materials Physics* **78**, 024428 (2008).
- [143] L. Wang and D.-X. Yao, *Physical Review B* **98**, 161403 (2018).
- [144] Y.-F. Chen and D.-X. Yao, *Physical Review B* **107**, 155129 (2023).
- [145] S. Li, Y. Xie, and Y. Chen, *Physical Review B* **104**, 085127 (2021).
- [146] M. N. Huda, S. Kezilebieke, and P. Liljeroth, *Physical Review Research* **2**, 043426 (2020).
- [147] C.-Y. Chen, E. Li, H. Xie, J. Zhang, J. W. Y. Lam, B. Z. Tang, and N. Lin, *Communications Materials* **5**, 54 (2024).